Streamwise inhomogeneity of spectra and vertical coherence of turbulent motions in a finite-size wind farm

Tanmoy Chatterjee [*]
General Electric (GE Global Research), Niskayuna, New York 12309, USA

Yulia T. Peet [†]
School for Engineering of Matter, Transport and Energy, Arizona State University, Tempe, Arizona 85287, USA

(Received 21 May 2020; accepted 19 October 2021; published 9 November 2021)

This paper examines the streamwise-inhomogeneous nature of turbulence in a finite-size developing wind farm. While previous analysis involving Fourier spectra revealed an interesting dynamics showing a dominance of the large-scale motions on the order of ten rotor diameters in the energetics of fully developed wind farms [T. Chatterjee and Y. T. Peet, Phys. Rev. Fluids **3**, 034601 (2018)], harmonic analysis methods do not capture the streamwise variability of spectra, especially important in strongly inhomogeneous flows such as a developing wind farm turbulence. The current study uses wavelet analysis of large eddy simulation data to investigate the turbulent spectra with respect to its spatial position along the wind farm. The analysis shows that the correlation length scales grow significantly past the first row of wind turbines, testifying to a strengthening of the large-scale motions by wind turbines. A vertical coherence of streamwise and vertical velocity fluctuations is also found to increase significantly past the first row of turbines, associated with the development of a global energy transfer mechanism between the outer layer and the wind turbine region. While this mechanism, known as a downdraft of kinetic energy, was previously discussed in the context of fully developed wind farms, the current study illustrates a signature of its origination after as early as the first row of wind turbines. Understanding of the mechanisms responsible for the reorganization of motions of different scales in wind farm flows is useful for designing efficient wind farm control strategies and mitigating the effects of the downstream wakes.

DOI: 10.1103/PhysRevFluids.6.114601

I. INTRODUCTION

Wind farms in atmospheric boundary layers (ABLs) pose a complex multiscale problem of interaction between the surface layer turbulence, the wake turbulence generated by wind turbines, and the outer layer motions [1]. The effect of this interaction is seen not only in the small scales of motion and the dynamics of the individual turbulent eddies, but also in the larger scales that set the stage for the global organization of turbulent motions in wind farms [2–4]. It was previously shown that fully developed wind farm flows demonstrate an existence of organized coherent motions with a significant spectral energy content in the length scales of around ten rotor diameters that also contribute to the energy production in wind farms [5–7]. These motions were associated with the

[*]tchatte3@asu.edu
[†]ypeet@asu.edu

vertical momentum transfer mechanisms between the outer layer and the rotor region of wind farms, known as the downdrafts of the mean kinetic energy (MKE) flux [7,8].

While the downdrafts were previously observed and discussed in the context of fully developed wind farms [7,8], the questions remain of "when" and "how" they are formed in realistic finite-size wind farms. Indeed, if the wind turbines are responsible for the increase of length scales and a potential reorganization of the turbulent motions as compared to a turbine-free atmospheric boundary layer, a detailed analysis of turbulence during the first several rows of a wind farm can potentially reveal the processes involved with such a reorganization.

Previous analysis of finite-size wind farms already highlighted the importance of streamwise-inhomogeneous mechanisms in both the flow topology and the energy harvest processes, such as internal boundary layer growth, development and merging of wind turbine wakes [9–12], and an interplay between streamwise advection and vertical MKE fluxes in the energy budget [13,14]. The current paper in particular focuses on the analysis of streamwise-dependent length scales of the turbulent energetic motions, so that a gradual change in structure and characteristic sizes of well-correlated eddies due to a placement of turbines can be investigated. This is done via a wavelet transform analysis of the corresponding streamwise-inhomogeneous signals, which allows us to obtain simultaneous information about the spectral content and the spatial location of the signal. Wavelet transform has a rich mathematical history [15,16] and has been developed into a robust tool in the last five decades for studying turbulence [17–19]. The current study can be contrasted with the previous studies devoted to a spectral analysis in wind farms, which were, however, done with Fourier-based methods [7,20]. Understanding the spatial variability and structure of the organized energetic motions in finite-size wind farms is important for design and control of finite-scale power generating facilities, as well as evaluation of the impact of wind farms on the surrounding communities [21,22]. This might be especially relevant in the context of an emerging distributed wind infrastructure paradigm [23], where small-scale power generating facilities are placed in living communities for local distributed power generation.

In the current paper, large eddy simulation (LES) data for a flow generated via an interaction of a 3×3 wind turbine (WT) array with a background neutral atmospheric boundary layer at $\mathrm{Re} \sim O(10^9)$ are analyzed using wavelet tools to investigate the streamwise inhomogeneity of spectra and vertical coherence in developing wind farm flows.

The LES of the 3×3 wind turbine array was originally introduced in our previous work [24,25]. The paper is organized as follows. In Sec. II, we discuss the computational setup and the grid design for the LES model, which generates the high-fidelity data for our present analysis. In Sec. III A, we present the definition and nomenclature of the wavelet transform. In Sec. III B, the limitations of the wavelet analysis and the interpretability of results are discussed. In Sec. IV, we present the main results concerning the wavelet spectra intermittency and the vertical coherence functions defined below. Conclusions are stated in Sec. V.

II. NUMERICAL METHODOLOGY

The numerical method implements a variational formulation of the Navier-Stokes (NS) equations involving a Galerkin projection using an open-source spectral element method (SEM) solver NEK5000 [26] in $\mathbb{P}_N - \mathbb{P}_{N-2}$ formulation (see [27] for more details). The simulations have been carried out in an LES framework [28] and the wind turbines are modeled using actuator lines [7].

A. Subgrid-scale model for large eddy simulations

The spatially filtered three-dimensional (3D) Navier-Stokes equations for LES of wind turbine arrays in a neutrally stratified ABL flow can be obtained by incorporating a convolution integral filter on the original Navier-Stokes equations:

$$\frac{\partial \widetilde{\mathbf{u}}}{\partial t} + \widetilde{\mathbf{u}}\nabla\widetilde{\mathbf{u}} = -\frac{1}{\rho}\nabla\widetilde{p^*} + \widetilde{\mathbf{F}}_x + \widetilde{\mathbf{F}}_{AL} + \nu\nabla^2\widetilde{\mathbf{u}} - \nabla\cdot\tau. \tag{1}$$

We use an (x, y, z) Cartesian coordinate system, where x corresponds to the streamwise direction, y to the spanwise direction, and z to the vertical (wall-normal) direction.

Here, $\widetilde{\mathbf{u}}$ is the filtered velocity vector, $\widetilde{p}^*$ is the modified pressure [29], and $\widetilde{\mathbf{F}}_x$ is the streamwise driving pressure gradient, while $\widetilde{\mathbf{F}}_{AL}$ represents the actuator line forces exerted by the rotating wind turbine blades. The subgrid stress (SGS) tensor in Eq. (1), $\tau = \widetilde{\mathbf{u}\mathbf{u}^T} - \widetilde{\mathbf{u}}\widetilde{\mathbf{u}}^T$ arising from the noncommutativity of filtering with the nonlinear advection term, is modeled using an algebraic wall-damped Smagorinsky-type eddy viscosity closure [28,30],

$$\tau^{SGS} - \tfrac{1}{3}\tau^{SGS}\delta_{kk} = -2(l_f)^2|\nabla^s\widetilde{\mathbf{u}}|\nabla^s\widetilde{\mathbf{u}}, \tag{2}$$

where $\nabla^s\widetilde{\mathbf{u}} = 1/2(\nabla\widetilde{\mathbf{u}} + \nabla\widetilde{\mathbf{u}}^T)$ and $|\nabla^s\widetilde{\mathbf{u}}| = (2\nabla^s\widetilde{\mathbf{u}} : \nabla^s\widetilde{\mathbf{u}})^{1/2}$ and the filter length scale is defined as $l_f^{-n} = (C_0\Delta)^{-n} + [\kappa(z + z_0)]^{-n}$ ($\kappa = 0.41$ is von Kármán constant, $z_0 = z_{0,lo}$ is aerodynamic roughness length of the bottom surface, $C_0 = 0.19$, $n = 0.5$). The grid size Δ in Eq. (2) is defined as $\Delta = (\Delta_x\Delta_y\Delta_z)^{1/3}$ (Δ_η is the grid size in the η direction defined as the local average between the Gauss-Legendre-Lobatto (GLL) node spacings to either side from a particular point in this direction [28]). The current choice of the SGS model represents a competent alternative to the dynamic-based procedures, since it is computationally efficient yet of a similar level of fidelity. The validation of this model in a neutral ABL framework for spectral elements can be found in [28].

B. Near-wall model

At the bottom surface, boundary conditions involve a wall stress vector $\boldsymbol{\tau}_s$ [31,32] being incorporated through the horizontal velocity vector data $\widetilde{u}_h$ at the first grid point using the standard Monin-Obukhov similarity law [33] along with no-penetration conditions of large eddies, $\widetilde{w} = 0$,

$$\frac{1}{\rho}\boldsymbol{\tau}_s = -\kappa^2\frac{\widehat{\widetilde{u}}_{h,\frac{\Delta z}{2}}(x, y, t)\left|\widehat{\widetilde{u}}_{h,\frac{\Delta z}{2}}\right|(x, y, t)}{\log\left(\frac{z}{z_0}\right)\Big|_{\frac{\Delta z}{2}}^2}, \quad \Delta z/z_0 \gg 1, \tag{3}$$

where $\widehat{\widetilde{\boldsymbol{u}}}_{h,\frac{\Delta z}{2}} = \widehat{\widetilde{u}}_{\frac{\Delta z}{2}}\vec{e}_x + \widehat{\widetilde{v}}_{\frac{\Delta z}{2}}\vec{e}_y$ ($\vec{e}_x, \vec{e}_y$ are unit vectors in the x, y directions) and $|\widehat{\widetilde{\boldsymbol{u}}}_{h,\frac{\Delta z}{2}}| = \sqrt{\widehat{\widetilde{u}}^2_{\frac{\Delta z}{2}} + \widehat{\widetilde{v}}^2_{\frac{\Delta z}{2}}}$. The "hat" represents an additional explicit filtering carried out in the modal space by attenuating the four highest Legendre polynomial modes out of $p = 7$ resolved modes of the spectral element model [28,34]. $\widehat{\widetilde{\boldsymbol{u}}}_{h,\frac{\Delta z}{2}}$ is calculated as an interpolation between the "wall" and Δz (the distance between the bottom boundary and the first GLL point from the boundary in the vertical direction).

C. Actuator line model

In an actuator line model [35], the blades with the aerofoil cross sections are divided into elements and the local lift (L) and drag (D) forces experienced by each element are calculated as $(L,\ D) = \frac{1}{2}C_{(l,d)}(\alpha)\,\rho\,V_{rel}^2\,c\,w_d$, where c and w_d are the chord length and the blade width, respectively. The local angle of attack, α, is computed from the relative velocity, V_{rel}, the streamwise velocity, u ($\tilde{u}$ in LES) and the pitch angle, γ. The local aerodynamic force is calculated as $\vec{f} = L\vec{e}_L + D\vec{e}_D$ (here $\vec{e}_L$ and $\vec{e}_D$ are the unit vectors in the direction of the local lift and drag, respectively). The total reaction force summed from all the N blade elements experienced by the fluid is distributed smoothly onto several mesh points and is given as the actuator line force in the NS equations (1),

$$\widetilde{\mathbf{F}}_{AL}(x,\ y,\ z,\ t) = -\sum_{i=1}^{N}\vec{f}(x_i,\ y_i,\ z_i,\ t)\,\eta_\epsilon(|\vec{r} - \vec{r}_i|), \tag{4}$$

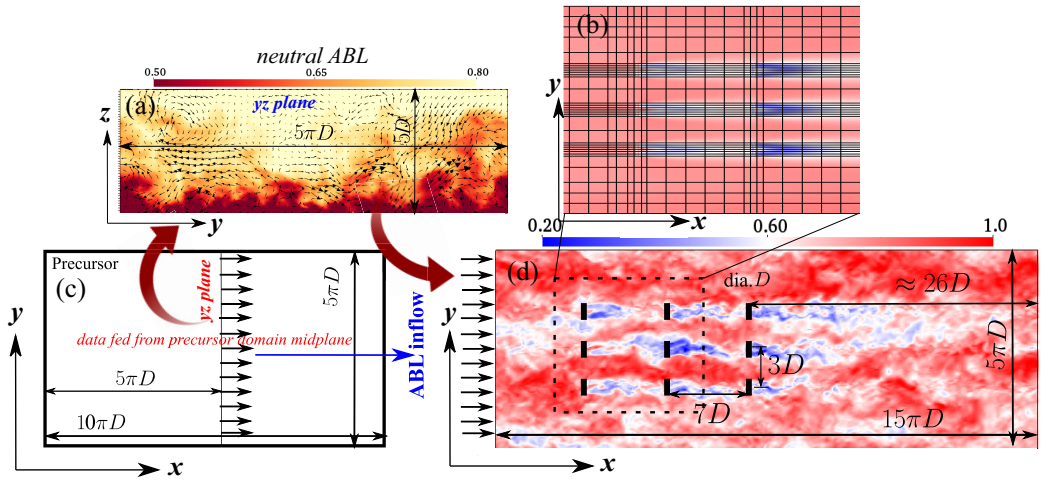

FIG. 1. A schematic of the computational setup featuring an ABL precursor feeding into a 3×3 wind turbine array region. Left: ABL domain, with xy view of the computational domain (c), and a typical ABL snapshot of the instantaneous u velocity in the yz plane (normalized by U_∞) superposed with in-plane v, w velocity vectors (a). Right: Wind turbine array domain, with xy view of the computational domain superposed with the instantaneous u/U_∞ velocity (d), and a close-up view of the WT domain around the turbine rotors (only the element boundaries are shown) with the temporally averaged u/U_∞ velocity (b).

where $\vec{r} = (x, y, z)$, (x_i, y_i, z_i) are the coordinates of the centers of the actuator blade elements at time t, and $\eta_\epsilon(d)$ is a Gaussian function in the form of $\eta_\epsilon(d) = 1/\epsilon^3\pi^{3/2}\exp[-(d/\epsilon)^2]$. $\epsilon = 2\,w_d$ is used in the current study as suggested in [35,36] for optimum results.

In the current actuator line simulations, Tjæreborg turbines have been used [35]. The lift and drag coefficients $C_l(\alpha)$, $C_d(\alpha)$ for the blades were taken from the National Advisory Committee for Aeronautics (NACA) 44xx series aerofoil wind tunnel measurements performed on NACA airfoils at a chord Reynolds number, $\mathrm{Re}_c = 6\times10^6$. The equivalent time-varying thrust coefficient of the turbines is in the range $C_T \sim 0.7$–0.8, which is similar to $C_T = 0.75$ used in the actuator disk model of [8]. Each actuator line is discretized using 30 uniformly sized blade elements (i.e., per rotor radius) as in [35]. The Actuator Line (AL) model is more advanced than the actuator disk model [2,8], commonly used in numerical computations of wind farms, in its capability to capture the tip vortices being shed in the near wake ([34,35]).

D. Computational setup

The computational setup consists of a neutral ABL precursor domain of size $10\pi D\times5\pi D\times5D$ scaled with the turbine rotor diameter D [28], and a wind farm domain of a size $15\pi D\times5\pi D\times5D$ containing a 3×3 array of wind turbines, with Fig. 1 showing a schematic of the setup and some typical flow snapshots. The ABL precursor simulations are driven by a pressure gradient forcing that ensures a constant mass flux, and the data from the midplane of the ABL precursor ($x = 5\pi D$) are spectrally interpolated [37] onto the grid points of the inflow plane of the wind farm domain, to serve as the inflow condition to the wind farm domain [24,38]. In the subsequent analysis, we will be referring to the inner and outer layers of the ABL. In accordance with the previous literature [39,40], we define the inner layer here as the region in and below the logarithmic layer, and the outer layer as the region above the logarithmic layer, where the velocity profile deviates from the logarithmic law, occurring at $z \geqslant 0.2H$ [39].

A 3×3 WT array domain is designed in concordance with the experimental setup described in [5,41] and has been introduced in a spectral element framework in our previous work ([24,25]).

TABLE I. Details of the computational grids for the precursor ABL and the wind turbine array domains. N_η^e is the number of spectral elements in the η direction. Eight GLL nodes have been used per element per Cartesian direction.

Case	Geometry	$N_x^e \times N_y^e \times N_z^e$	Grid points
Neutral ABL	$10\pi D \times 5\pi D \times 5D$	$30\times20\times24$	5.06×10^6
WT array	$15\pi D \times 5\pi D \times 5D$	$48\times32\times24$	1.281×10^7

The first row of three rotors is placed at $\pi H/2$ distance from the inflow boundary ($H = 5D$ is the ABL thickness), which is equivalent to $7.85D$. The streamwise distance between the turbines is $7D$, while the spanwise distance is $3D$. The hub height of the turbines is at $z_h = D = 0.2H$, i.e., at the lower 20% of the ABL. The hub-height location is designed in such a way that the bottom tip, $z_h - D/2 = 0.1H$, lies in the inner layer, while the top tip of the rotor, $z_h + D/2 = 0.3H$, lies in the outer layer of the ABL. Wind turbines rotate with a tip-speed ratio $\lambda_R = 5$, where tip-speed ratio is defined as $\lambda_R = \omega R/U_h$, where U_h is the mean wind speed of the incoming ABL flow at hub height z_h, R is the radius of the turbine rotor, and ω is the rotor speed in rad/s. A stabilized outflow boundary condition [42] has been used for the outflow of the wind turbine domain which is $\sim 26D$ away from the third row of the turbines. The blockage ratio for the wind farm domain is 3% [43]. Grid details of the neutral ABL and the WT array domains are documented in Table I. Both grids feature the SEM polynomial order $p = 7$ which corresponds to eight GLL points within the element. The grid resolution

$$\Delta_\eta^e = L_\eta^e / p, \tag{5}$$

where L_η^e is the width of the element in the η direction, is documented in Table II for both ABL and WT array domains. Since the grid resolution defined in this way is an element-dependent quantity, the maximum, minimum, and the average values of the Δ_η^e within each grid are presented in Table II. It is seen that, while the ABL grid features a uniform distribution of elements in all three directions, the WT array grid is refined in the rotor swept area in the yz plane, as well as immediately upstream and downstream of the turbine rotors in the streamwise direction. A close-up of the spectral element grid (without the GLL points) near the wind turbines for the WT array is shown in Fig. 1 for a reference.

A velocity scale U_∞ is defined as the mean wind velocity above the canopy, calculated as the time-averaged and horizontally averaged streamwise velocity above the WT array (at the top domain boundary). With the velocity scale U_∞, and the length scale D, the Reynolds number of the simulations is $\sim 10^9$. After achieving statistical stationarity, the simulations have been carried out for 800 flow through times T_e to collect statistics ($T_e = 15\pi D/U_\infty$). Statistics were calculated using $\approx$ 16000 snapshots that were placed $1/20\,T_e$ apart. Statistical decorrelation of snapshots and convergence in the large scales was ensured with this choice of temporal separation and the number of snapshots.

TABLE II. Maximum, minimum, and average grid sizes for the ABL and the wind turbine array domains.

	Neutral ABL			WT array		
Direction	$\Delta_{\eta\,\max}$	$\Delta_{\eta\,\min}$	$\overline{\Delta}_\eta$	$\Delta_{\eta\,\max}$	$\Delta_{\eta\,\min}$	$\overline{\Delta}_\eta$
x	$0.1496D$	$0.1496D$	$0.1496D$	$0.1683D$	$0.0472D$	$0.1402D$
y	$0.1120D$	$0.1120D$	$0.1120D$	$0.1658D$	$0.0179D$	$0.0701D$
z	$0.0298D$	$0.0298D$	$0.0298D$	$0.0471D$	$0.0238D$	$0.0298D$

III. ANALYSIS METHODOLOGY

A. Definition and nomenclature of wavelet transform

1. Wavelet transform

The wavelet transform can be defined as a convolution of the function in physical space with the basis function dependent on a spatial location and a scale. The basis function of the wavelet transform is $\psi \in L_2(\mathbb{R})$ which satisfies the admissibility condition as

$$C_\psi = \int_{-\infty}^{\infty} \frac{|\hat{\psi}(k_x)|^2}{|k_x|} \mathrm{d}k_x < \infty, \tag{6}$$

where $\hat{\psi}(k_x)$ is the one-dimensional (1D) Fourier transform of ψ.

For the turbulent fluctuating velocity field $u_i'(x, y, z, t)_{i=1,\ldots,3} \in \Omega(\mathbb{R}^3, [0, \infty) \cap L_2(\mathbb{R}^3))$, the wavelet transform of u_i', i.e., $\mathcal{W}_\psi[u_i'](a, b)_{i=1,\ldots,3} \in \Omega(\mathbb{C}^3, [0, \infty) \cap L_2(\mathbb{R}^4))$ can be given as

$$\mathcal{W}_\psi[u_i'](a, b, y, z, t) = \int_{-\infty}^{\infty} u_i'(x, y, z, t)\psi_{a,b}^*(x)\mathrm{d}x, \tag{7}$$

where $\psi_{a,b}(x) = \frac{1}{\sqrt{|a|}}\psi(\frac{x-b}{a})$ is obtained by translating and dilating the mother wavelet.

We now replace a (scale) and b (translation) by the variables

$$\widetilde{k}_x = k_\psi/a, \quad \widetilde{x} = b, \tag{8}$$

to distinguish them from the variables without the tilde (k_x, x) used in Fourier and physical space, respectively. Here, k_ψ is the centroid wavenumber of the mother wavelet [18,44] and is defined by

$$k_\psi = \frac{\int_{-\infty}^{\infty} k_x|\hat{\psi}(k_x)|^2\mathrm{d}k_x}{\int_{-\infty}^{\infty} |\hat{\psi}(k_x)|^2\mathrm{d}k_x}. \tag{9}$$

A space-dependent energy spectrum can be defined as a function of $(\widetilde{x}, \widetilde{k}_x)$ [45]:

$$\widetilde{E}_{u_i'}(\widetilde{k}_x, \widetilde{x}, z) = \frac{1}{k_\psi C_\psi} \int_{-\infty}^{\infty} \left\langle \left| \{\mathcal{W}_\psi[u_i'](k_\psi/\widetilde{k}_x, \widetilde{x}, y, z, t)\} \right|^2 \right\rangle_T \mathrm{d}y. \tag{10}$$

It can be shown [46,47] that a streamwise integration of the wavelet energy spectra, $\widetilde{E}_{u_i'}(\widetilde{k}_x, z) = \int_{-\infty}^{\infty} \widetilde{E}_{u_i'}(\widetilde{k}_x, \widetilde{x}, z)\mathrm{d}\widetilde{x}$, is equivalent to a bandpass filtering of a Fourier energy spectrum $E_{u_i'}^F(k_x, z)$, premultiplied by the inverse of the wavenumber $\widetilde{k}_x$,

$$\widetilde{E}_{u_i'}(\widetilde{k}_x, z) = \frac{1}{\widetilde{k}_x C_\psi} \int_{-\infty}^{\infty} E_{u_i'}^F(k_x, z)|\hat{\psi}(k_x k_\psi/\widetilde{k}_x)|^2\mathrm{d}k_x, \tag{11}$$

a fact that will be further used for the validation of the wavelet transform.

2. Morlet wavelet

The wavelet used in the subsequent energy spectral analysis is an analytical Morlet wavelet [48]. The analytical Morlet wavelet (a complex exponential with a real Gaussian window) and its Fourier transform can be defined as [44,49]

$$\psi(x) = \exp(ik_0 x - x^2/2), \tag{12}$$

$$\hat{\psi}(k_x) = \sqrt{2\pi}\exp\left(-\tfrac{1}{2}(k_x - k_0)^2\right). \tag{13}$$

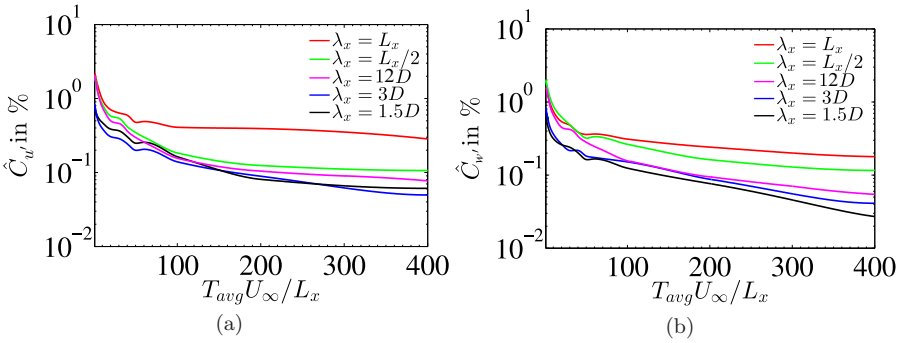

FIG. 2. Coefficient of variation $\hat{C}$ of streamwise spectra at various averaging times. (a) $\hat{C}_{u'}$, (b) $\hat{C}_{w'}$. $L_x = 15\pi D$ is the streamwise length of the WT array domain.

The peak wavenumber for the wavelet can be obtained from the roots of $d\hat{\psi}/dk_x = 0$, which is k_0 for the Morlet wavelet from Eq. (13). In this work, we use the peak wavenumber $k_0 = 2\pi$. Since the scale to wavenumber frequency in wavelet transform is given by $a = k_\psi/\tilde{k}_x$, where k_ψ is calculated by Eq. (9), from [49] we find that $a = \frac{k_0+\sqrt{2+k_0^2}}{2\tilde{k}_x}$, which gives the Fourier wavelength $\tilde{\lambda}_x = 2\pi/\tilde{k}_x \approx a$ for $k_0 = 2\pi$. Note that the centroid wavenumber $k_\psi = \frac{k_0+\sqrt{2+k_0^2}}{2}$ is very close to the peak wavenumber k_0. The Morlet wavelet obeys the "localization" property; for example, its Fourier transform $\hat{\psi}(k_x)$ and its derivatives decay rapidly as the wavenumber $k_x \to \infty$ [50]. High-order moments of the Morlet wavelet are nearly zero for $k_0 = 2\pi$ [48].

In the subsequent analysis, the symbol tilde used to denote the wavenumber associated with the wavelet scale, $\tilde{k}_x = k_\psi/a$, will be omitted for brevity.

B. Limitations of analysis and interpretation of results

1. Statistics of large scales

In this section, the fidelity of the statistics for large scales of motion is illustrated. Large scales are defined here as the scales of the order of ten rotor diameters, $O(10D)$, or one boundary layer height H, and must be contrasted with large-scale and very-large-scale motions observed in the outer layer in wall turbulence, which reach the lengths of several boundary layer heights [51,52]. The large scales of motion have long representative time scales and can potentially have fewer decorrelated snapshots, necessitating caution while obtaining statistical convergence. To assess the sensitivity of large-scale statistics to the averaging time, we calculate the uncertainty of the planar averaged and temporally filtered streamwise and spanwise energy spectra at different wavelengths. The spectra can be given as

$$\langle \tilde{E}_{u_i'} \rangle_{y,z,T_{\text{avg}}} = \frac{1}{T_{\text{avg}}} \int_0^{T_{\text{avg}}} \left[\frac{1}{L_y L_z} \int_{y_{\min}}^{y_{\max}} \int_{z_{\min}}^{z_{\max}} u_i'(y, \lambda_x, z, t)^* u_i'(y, \lambda_x, z, t) \mathrm{d}y \mathrm{d}z \right] \mathrm{d}t. \tag{14}$$

Note that the spectra are a function of the temporal averaging (filtering) time T_{avg} and in the limit $\lim_{T_{\text{avg}} \to \infty} \langle \tilde{E}_{u_i'} \rangle_{y,z,T_{\text{avg}}} = \langle \bar{E}_{u_i'} \rangle_{y,z}$, the spectra approach a true, infinite-time average. The uncertainty in the averaging time is calculated from the coefficient of variation with respect to different consecutive time series of the duration $t = T_{\text{avg}}$ (standard deviation normalized by the arithmetic mean of the energy spectra corresponding to velocity u_i'), $\hat{C}_{u'}(\lambda_x, T_{\text{avg}})$ and $\hat{C}_{w'}(\lambda_x, T_{\text{avg}})$, and is documented in Fig. 2. The plots in Figs. 2(a) and 2(b) illustrate a fast decay in the coefficient of variation with increasing T_{avg}, which slows down after approximately 100 flow-through times. It is seen that the decay in the largest resolved scales of motion, $\lambda_x = L_x$, on the order of the domain length, is fairly

slow and does not reach an acceptable level of statistical invariance for a duration of 400 flow-through times, which is half of the total simulation time. After 400 flow-through times, length scales of the order of $\lambda_x = L_x/2$ show reasonable levels of invariance for the streamwise velocity, but not for the vertical velocity. In this paper, we thus focus our analysis on length scales with the upper bound of $\lambda_x = 12D$. We choose this value as an upper bound, because the uncertainty for $\lambda_x = 12D$ scales after 400 flow-through times is less than 0.1% for both u' and w' velocities: $\max_{T_{\text{avg}}} \hat{C}_{u'} \lesssim 0.1\%$, $\max_{T_{\text{avg}}} \hat{C}_{w'} \lesssim 0.1\%$, which speaks of a sufficient convergence of the spectra. Note that the total averaging time for the results presented in this paper ($T_{\text{avg}} = 800\,T_e$) is twice the maximum sampling time for the calculation of the coefficient of variation ($T_{\text{avg}} = 400\,T_e$), since the latter in the current analysis was calculated by subdividing all the available snapshots into disjoint subgroups, with a maximum size of $400\,T_e$.

2. Resolution at small scales

The smallest scale that can be analyzed with the wavelet transform depends on the resolution of the LES grid. It is thus instructive to estimate the length scales (wavelengths) that can be captured by the current numerical grid. Per the Nyquist criterion, the resolved wavelength threshold, $\lambda_{\eta,\text{res}}$, can be defined as twice the corresponding grid resolution, which, as discussed above, in the SEM can be represented by an average GLL node distance within the element, Δ^e_η defined by Eq. (5):

$$\lambda^e_{\eta,\text{res}} = 2\,\Delta^e_\eta. \tag{15}$$

As evident from the discussion in Sec. II D and Table II, the WT array grid resolution is nonuniform, capturing finer scales in the proximity of wind turbine rotors, and larger scales further away from the turbines. Correspondingly, the minimum, maximum, and average wavelengths captured by a streamwise wavelet transform on the WT grid, as analyzed in this paper, are $\lambda_{x,\text{res max}} = 0.3366D$, $\lambda_{x,\text{res min}} = 0.0944D$, and $\overline{\lambda}_{x,\text{res}} = 0.2804D$. Please note that this definition of the resolved wavelengths only takes into consideration the variability in the size of spectral elements and not the variability of the GLL node clustering within an element. This definition aims to reconcile the high-order approximation defined on spatially varying GLL points, and the classical spectral approximation prototypical with the uniform grids. All spectral results in the following analysis refer to the wavelengths above $0.6D$, which is larger than the spectral grid resolution limit of $\lambda_{x,\text{res max}} = 0.3366D$ found in the far wake of wind turbines.

C. Choice of wavelets and validation versus Fourier spectra

For a reliable representation of the turbulent spectra and length scales, it would be desirable to demonstrate the relative independence of the results on the chosen convolution (wavelet) function. Additionally, The readers should take a note of Fig. 3 to consider the cone of influence (COI) in the wavelet transform, where the results are not trustworthy and influenced by domain boundaries. All wavelet spectral results demonstrated in the paper are out the COI. In Fig. 4, the energy spectra obtained with Morlet wavelet (used in this paper) and the Morse wavelet are compared at several streamwise stations around the second row of turbines. The plots in Fig. 4 illustrate that small scales less than the rotor diameter manifest a dependency of the computed spectra on the wavelet kernel, while the larger scales appear to be fairly indifferent to the wavelet function used. Since the scales analyzed in the current paper are greater than $0.6D$, a particular choice of the wavelet kernel is not expected to have a major influence on the results presented.

The two wavelets are further compared and validated versus the Fourier spectra by looking at a streamwise-integrated wavelet energy spectra with respect to the Fourier spectra in Fig. 5. From Eq. (11), one can see that the streamwise-integrated wavelet spectrum is essentially equivalent to a bandpass filtered Fourier spectrum, which is confirmed in the current results. All the typical scaling laws in the inner layer are captured well by both the wavelet and the Fourier spectra, albeit agreement between the Morlet wavelet and the Fourier results is slightly better than for the

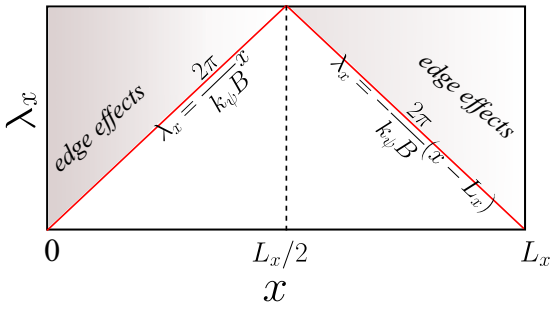

FIG. 3. Schematic of the cone of influence (COI) in a wavelet transform plot. Red lines, boundaries of the COI of the domain edges. Gray area, within the COI of the domain edges, edge effects dominant; white area, outside of the COI of the domain edges, free from edge effects; $[-B, B]$, compact support of the mother wavelet; k_ψ, centroid wavenumber of the mother wavelet.

Morse wavelet, perhaps, owing to the fact that the Morlet wavelet has more higher-order vanishing moments than the Morse wavelet [50,53].

IV. RESULTS

A. Streamwise correlation length scales

To document a streamwise inhomogeneity of a developing wind farm flow, we first present the streamwise correlation length scales in Fig. 6, which shows the correlation length scales for streamwise and vertical velocity fluctuations in the rotor region $z = z_h \pm D/2$, and in the outer layer. Correlation length scales are calculated as the integral of the correlation function,

$$\mathcal{L}_\zeta(x, z) = \int_{-\Delta_{x,C}}^{\Delta_{x,C}} \rho_\zeta(x, \Delta_x, z)\mathrm{d}\Delta_x, \tag{16}$$

with $\Delta_{x,C}$ being the cutoff location, where the correlation reaches the maximum negative value. To obtain the streamwise-varying correlation function, we use the windowing technique to ensure statistical convergence of the correlations as

$$\rho_\zeta(x, \Delta_x, z) = \int_{x-\mathcal{W}/2}^{x+\mathcal{W}/2} \langle \zeta(x', y, z, t)\zeta^*(x' + \Delta_x, y, z, t)\rangle_{y,T}\mathrm{d}x' \;\; \forall \zeta = u', w', \tag{17}$$

where $\mathcal{W}$ is the window size. Windows are allowed to overlap by 40%.

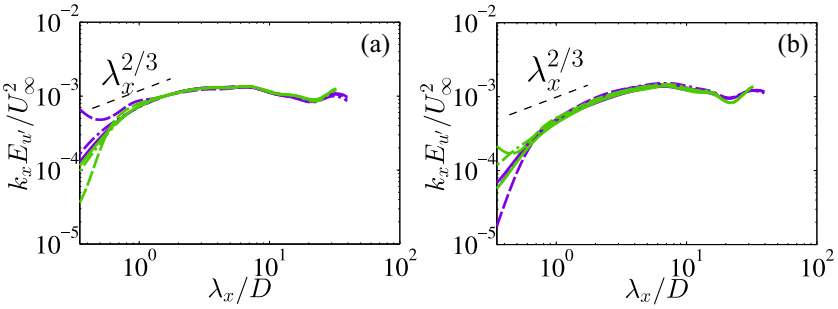

FIG. 4. Validation of the wavelet transform: comparison of a streamwise-varying spectra, $k_x\widetilde{E}_{u'}(\lambda_x, x)/U_\infty^2$, between Morlet and Morse wavelets, at different streamwise stations around the second row of turbines: solid line, $x_t + 0.1D$; dashed line, $x_t + 5D$; dash-dotted line, $x_t + 6.9D$; $x_t = 14.85D$ is the location of the second row of turbines. (a) $z = 0.125D$, (b) $z = z_h + D/2$. Green, Morlet wavelet; violet, Morse wavelet.

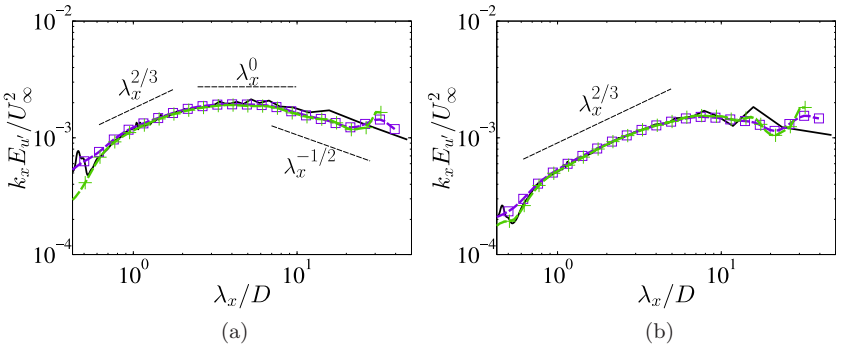

FIG. 5. Validation of the wavelet transform: comparison of a streamwise-integrated spectrum, $k_x\widetilde{E}_{u'}(\lambda_x)/U_\infty^2$, between Morlet and Morse wavelets and a Fourier transform. (a) $z = 0.125D$, inner layer; (b) $z = z_h + D/2$, top tip of the rotor. Green $+$, Morlet wavelet spectra; violet $\square$, Morse wavelet spectra; solid black, Fourier spectra.

The streamwise growth of the correlation length scales as depicted in Fig. 6 is pronounced in the wind turbine array region, especially for streamwise velocity fluctuations and the vertical velocity in the outer layer. This illustrates that the wind turbines interacting with the atmospheric boundary layer promote the development of larger-scale motions, especially in the outer layer. These motions in the outer layer are also characterized by strong streamwise correlations in vertical velocity that are likely associated with the downdrafts of kinetic energy in wind farm flows observed previously [7,8]. Correlations in streamwise velocity decrease past the second row of turbines at all vertical locations, testifying to a dominance of small-scale processes associated with the mixing in the wake region. Interestingly, a similar decrement of integral length scales downstream of turbine rotors was also observed in [54]. A secondary growth of streamwise length scales past the wind turbine array region at the hub height is also noted, potentially testifying to a recovery of large-scale eddies spurred by wind turbine interactions once they pass the region of a strong near-wake mixing.

The energetic mixing processes and the correlation length scales in a wind farm and a subsequent wake can be dependent upon the wind turbine operational parameters and the wind farm geometrical layout. In Appendix A, we document the influence of some of these parameters (such as a tip-speed ratio and a streamwise distance between the turbines) on the correlation length scales. The main conclusion from this study is that both the higher tip-speed ratios and the smaller interturbine distances increase the growth of the energetic large-scale motions and, at the same time, amount to a higher streamwise variability of length scales inside the wind farm domain due to stronger mixing effects.

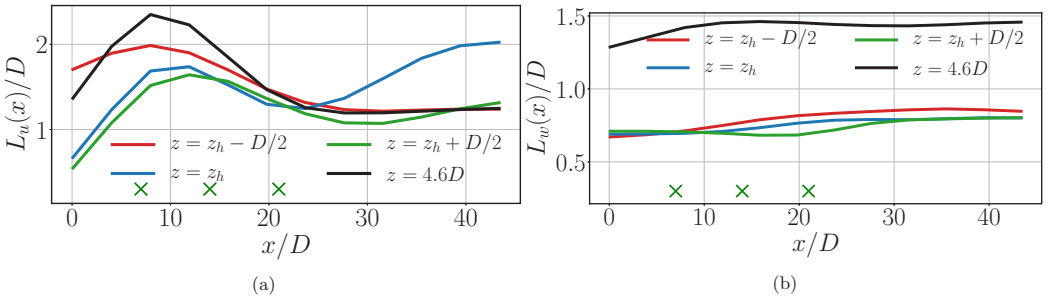

FIG. 6. Moving window correlation-based length scales, Eq. (17), at different heights (a) L_u and (b) L_w. Window size is $0.45L_x$ (L_x is the streamwise length of the domain); overlap is 40%.

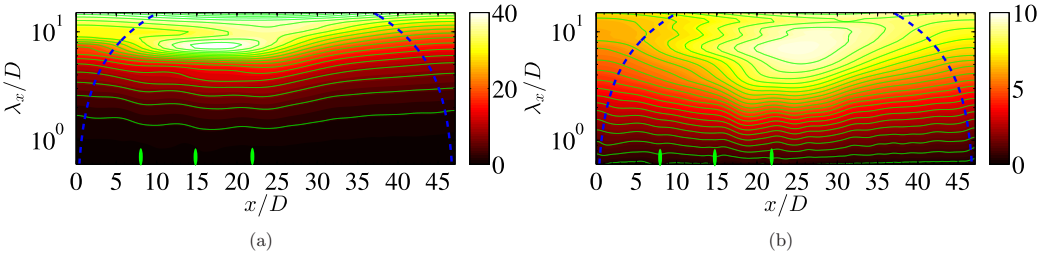

FIG. 7. Contour maps of wavelet energy spectra, (a) $E_{u'} \times 10^5$ and (b) $E_{w'} \times 10^5$ at hub-height $z = z_h$. Maps are overlaid with the contour lines in green. Green markers, streamwise location of the turbine rows.

B. Wavelet spectra and intermittency

1. Intermittency of velocity fluctuations

We begin this section by highlighting the u', w' wavelet spectra at the hub height, $z = z_h$ (Fig. 7), which illustrate the peak in energy in the turbine rotor regions. It can be seen that the spectra indicate the following picture:

(1) The streamwise spectral energy content [Fig. 7(a)] peaks within the wind farm region at about the length scales $\sim 7D$. These scales ($\sim 7D$) are indicative of the interturbine distances, and they, expectedly, dominate the size of the streamwise coherent motions in the wake region. Beyond the wind farm, the structures are no longer being broken down by the turbines, so that the length scales of the streamwise energy-containing eddies grow to $\gtrsim 10D$.

(2) For the vertical spectra [Fig. 7(b)], the peak is at similar length scales, but occurs slightly downstream of the turbine rows. It is also interesting to note that the region of the energetic length scales in the vertical direction is generally broader, with the range of scales between $3D$ and $10D$ involved, which were previously shown to be important in the energy production by wind farms [7].

To better understand the spatial variability of the wavelet energy spectra, we document the intermittency function of u', w' energy spectra [18,44] in the streamwise direction defined as

$$I_\xi(\lambda_x, x, z) = \frac{\widetilde{E}_\xi(\lambda_x, x, z)}{\frac{1}{L_x}\int_{x_{\min}}^{x_{\max}} \widetilde{E}_\xi(\lambda_x, x, z)\mathrm{d}x}, \tag{18}$$

where $\xi = u', w'$ are the streamwise and wall-normal turbulent velocity fluctuations, respectively, and L_x is the streamwise length of the domain. This definition is along the lines of [55] and is a measure of the deviation of the energy spectra at different streamwise locations from its streamwise integrated mean. In the context of the current paper, the intermittency function illustrates the degree of spatial variability of the kinetic energy and other statistical variables due to the presence of wind farms, which is indicative of a local departure from statistical homogeneity.

Figure 8 documents the streamwise intermittency of the wavelet energy spectra in and above the turbine rotor region ($z = z_h - D/2, z_h, z_h + D/2$). The gray patch in the plots corresponds to the region of "edge effects" owing to the cone of influence of the wavelet coefficients at the maximum wavelength plotted, $\lambda_x = 12D$. Evidently, wavelet coefficients corresponding to smaller wavelengths have a smaller region of influence (refer to Fig. 3). For smaller scales $\lesssim 12D$, colored markers are also provided denoting the boundaries of the cone of influence. Figure 8 illustrates that the maximum variability of the streamwise spectra at the hub height manifests itself in the length scale of $\lambda_x = 7D$, which is the streamwise distance between the rows of turbines. Above the hub height, we see an equivalent increase in the energy content over a broad range of length scales, while below the hub height it is only the small scales which manifest a high degree of variability. The peaks in small scales, which are seen in all locations through the turbine rotor region in both u' and w' spectra, roughly correspond to the streamwise location of wind turbines. Increased production of the kinetic energy in the small scales behind the turbine rotors is consistent with the recent investigation

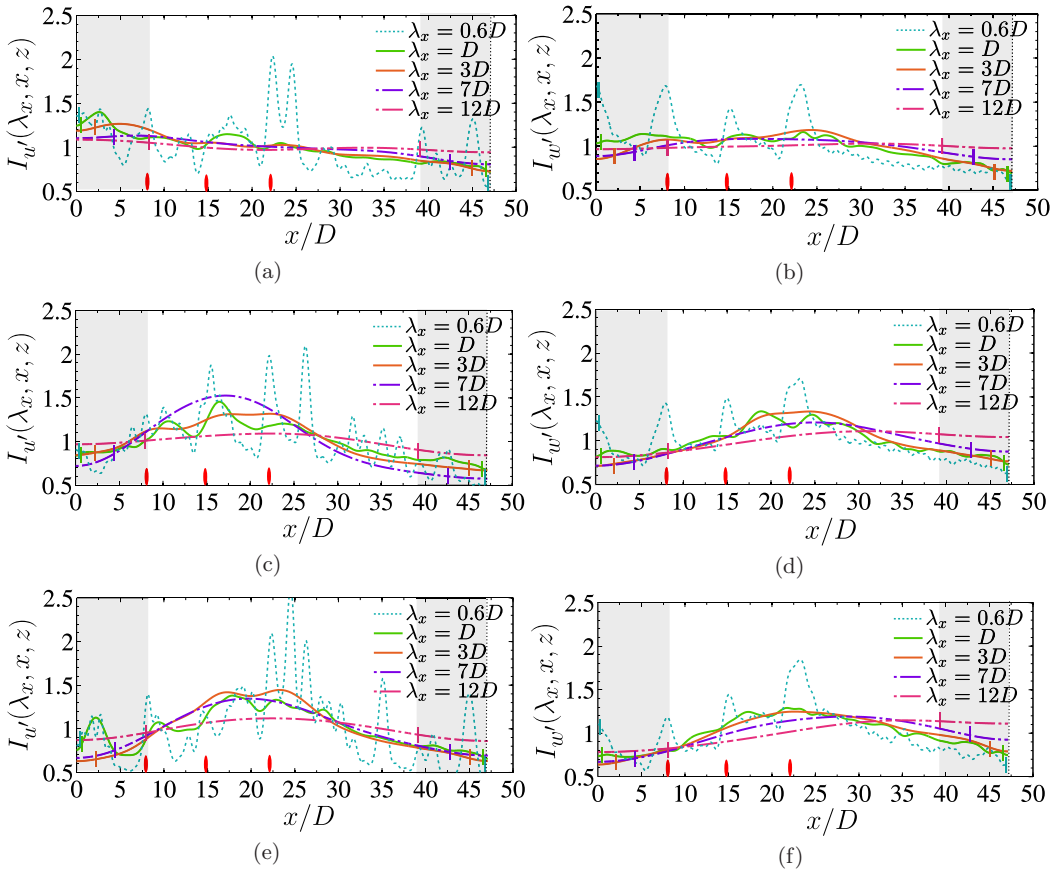

FIG. 8. Streamwise intermittency function for (a), (c), (e) u' velocity, $I_{u'}(\lambda_x, x, z)$, and (b), (d), (f) w' velocity, $I_{w'}(\lambda_x, x, z)$. (a), (b) $z = z_h - D/2$, bottom tip of the rotor; (c), (d) $z = z_h$, hub height of the rotor; (e), (f) $z = z_h + D/2$, top tip of the rotor, for different length scales using Morlet wavelets. Gray patch, region inside the cone of influence (COI) of the wavelet for the maximum wavelength considered, $\lambda_x = 12D$. Marks of the same color as the plots are bounds of the COI of the respective length scales. Red ellipses, streamwise location of the turbine rows.

[54] that demonstrated the decreased values of the correlation function and decreased integral length scales of streamwise velocity fluctuations behind the turbines. This observation is consistent with the behavior of the mixing length scales presented in Appendix A, which shows an increase in length scales upstream of turbine rotors and a marked decrease downstream thereof.

It is interesting to note a steady decay in all scales of motion for the $I_{u'}$ function in the bottom tip location of the rotor [Fig. 8(a)], indicating that there is a gradual drop in the streamwise energy spectra as one moves downstream throughout the wind farm array. A suppression of turbulence behind the bottom tip of the rotors and close to the ground was previously observed in [9,56,57].

The variation registered in the intermittency function occurs due to the presence of wind turbines. This is evidenced by the absence of such variations in a domain without wind turbines, analyzed in Appendix B. In particular, in Appendix B, we compare the wavelet u' and w' energy spectra of a 3×3 wind farm with the case of a neutral ABL without wind turbines. From this comparison, the modulation of different scales of motion by the wind farm as compared to a neutral ABL flow is further highlighted, and the interested readers are referred to Appendix B for this information.

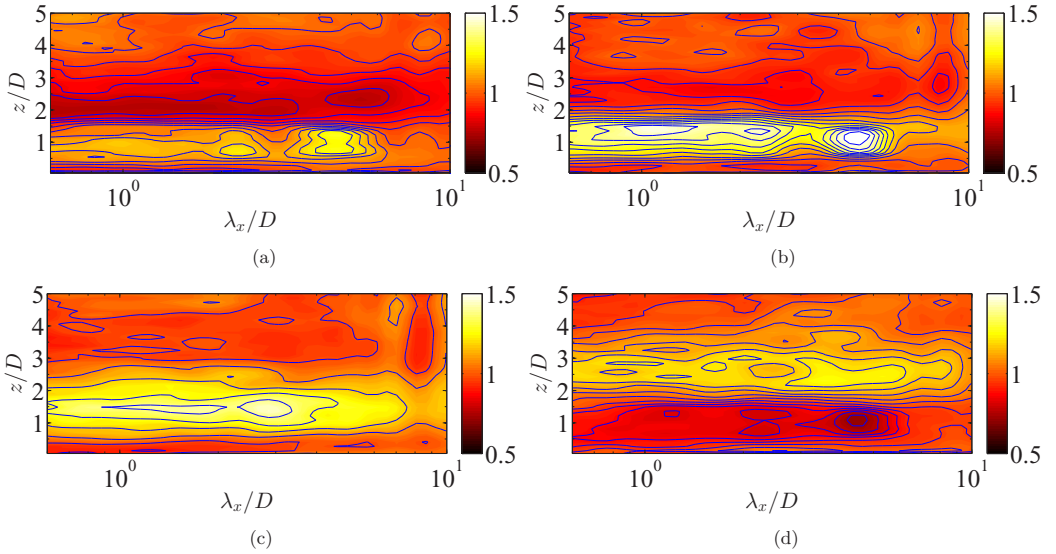

FIG. 9. Vertical variation of the intermittency function $I_{tke}(\lambda_x, x, z)$ of the turbulent kinetic energy wavelet spectra at various streamwise locations: (a) $x = x_{R,1} + 2D$, (b) $x \approx x_{R,2} + 2D$, (c) $x \approx x_{R,3} + 2D$, and (d) $x \approx x_{R,3} + 14D$ (downstream of the wind farm). $x_{R,i}$, location of the ith row of turbines.

2. Intermittency of kinetic energy

The spatial variability of the spanwise and temporally averaged kinetic energy wavelet spectra as a function of streamwise and wall-normal locations is documented in this section. The intermittency function of the kinetic energy wavelet spectra, defined as

$$I_{tke}(\lambda_x, x, z) = \frac{\widetilde{E}(\lambda_x, x, z)}{\frac{1}{L_x}\int_{x_{\min}}^{x_{\max}} \widetilde{E}(\lambda_x, x, z)\mathrm{d}x}, \tag{19}$$

is illustrated in Fig. 9. A peak of intermittency is observed at length scales $\lambda_x \sim 7D$ around the hub height, $z/D \sim 1$, shortly downstream of the first row of turbines [Fig. 9(a)]. After the second row of turbines, high intermittency is observed at all scales below $7D$ at hub height, and the region of high intermittency also spreads slightly above and below hub height. This is indicative of a vertical mixing of wind turbine wakes, as well as a growth of the internal boundary layer. After the third row of turbines, the zone of high intermittency is extended even further into the vertical direction. Downstream of the wind farm, in Fig. 9(d), the intermittency at the hub-height level is low, presumably due to a wake diffusion. However, the region above the turbine rotors, $z/D \sim 3$, shows high intermittency at all scales. The upward shift of the region of high intermittency with the downstream distance can possibly be associated with the updrafts of the large-scale structures generated in the wake by the large-scale motions.

C. Vertical coherence

1. Vertical coherence of the velocity fluctuations

The dynamics of the large scales in the WT array are further illustrated by the temporally averaged wall-normal correlations of the wavelet transform of the signals. The "coherence" [58,59] of the wavelet-transformed signals of the turbulent fluctuating velocity u_i' at two wall-normal z, z'

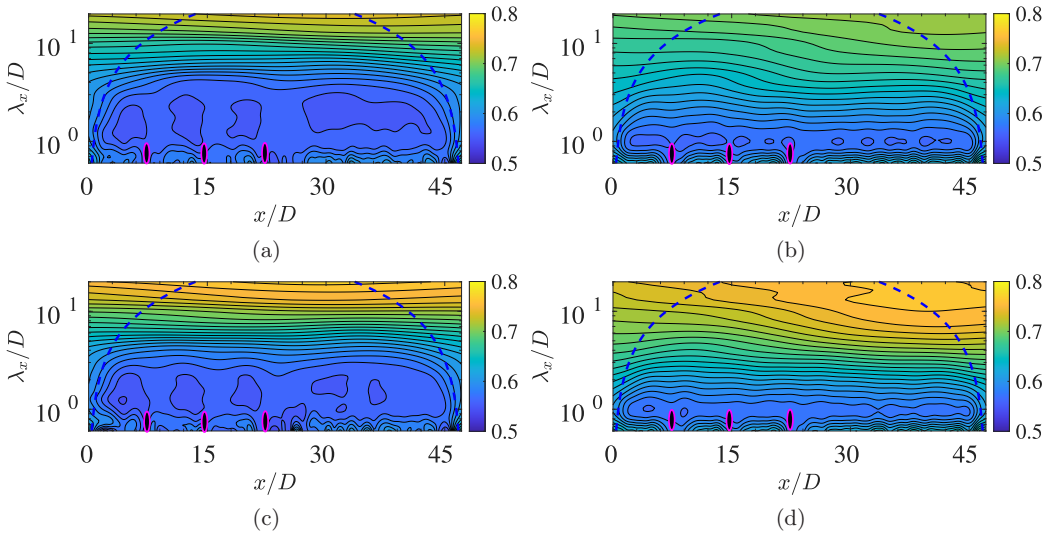

FIG. 10. Wavelet spectral vertical coherence of streamwise velocity u' (left) and wall-normal velocity w' (right) in the rotor region, $\rho_{\mathcal{W}_\psi[u_i',u_i']}(k_x, x, z, z')$. (a), (c) u' coherence. (b), (d) w' coherence. (a), (b) $z = z_h$, $z' = z_h - D/2$; (c), (d) $z = z_h$, $z' = z_h + D/2$. Black amd pink markers, streamwise location of the turbine rows. Blue dashed line, boundary of the COI.

locations can be defined as a correlation coefficient:

$$\rho_{\mathcal{W}_\psi[u_i',u_j']}(k_x, x, y, z, z', t) = \frac{|\mathcal{W}_\psi^*[u_i'](k_x, x, y, z, t)\mathcal{W}_\psi[u_j'](k_x, x, y, z', t)|}{|\mathcal{W}_\psi[u_i'](k_x, x, y, z, t)||\mathcal{W}_\psi[u_j'](k_x, x, y, z', t)|}. \tag{20}$$

In the current paper, we use the temporally and spanwise-averaged wavelet coherence as

$$\rho_{\mathcal{W}_\psi[u_i',u_j']}(k_x, x, z, z') = \frac{1}{L_y}\int_{y_{\min}}^{y_{\max}} \langle \rho_{\mathcal{W}_\psi[u_i',u_j']}(k_x, x, y, z, z', t)\rangle_T \mathrm{d}y. \tag{21}$$

A study of z-directional (vertical) coherence of the u', w' velocities is essential towards understanding how the flow is reorganized with respect to the vertical motions related to energy updrafts and downdrafts. Figure 10 shows the spectral vertical coherence of u', w' fluctuations in the streamwise location and streamwise wavenumber plane with correlations at $z = z_h$, $z' = z_h \pm D/2$. The vertical coherence function indicates that the eddies at hub height are better correlated in the wall-normal direction with the eddies near the top tip [Figs. 10(c) and 10(d)] than with the eddies near the bottom tip of the rotors [Figs. 10(a) and 10(b)]. Further, the u' coherence is fairly uniform with respect to a streamwise location in the large length scales $\lambda_x \sim O(10D)$, while the w' coherence increases as we move towards the downstream of the wind farm. This might be a manifestation of the processes responsible for reorganization of the large-scale structures downstream of the turbines favoring stronger coherent vertical motions associated with the downdrafts, that are growing stronger as the wind farm flow develops, and continue to evolve downstream of wind farm.

In Fig. 11, the u' and w' spectral vertical coherence is shown in the streamwise location and wavenumber plane for the correlations calculated in the outer layer, $z = z_o$, $z' = z_o + D/2$. At large scales, $\lambda_x \sim O(10D)$, the u' spectral vertical coherence remains similar in magnitude as a coherence in the rotor region, while the w' coherence in the outer layer increases by approximately 5% compared to the rotor region. High coherence of the vertical velocity in the outer layer points to a strong influence of the downdraft motions on the outer layer dynamics that contributes to the energy transfer between the outer layer and the wind turbine region.

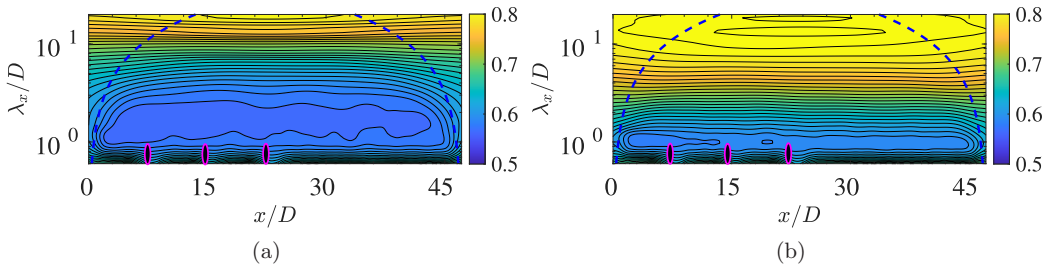

FIG. 11. Wavelet spectral vertical coherence of streamwise velocity u' (left) and wall-normal velocity w' (right) in the outer layer, $\rho_{\mathcal{W}_\psi[u'_i,u'_j]}(k_x, x, z, z')$. (a) u' coherence and (b) w' coherence. $z = z_o$, $z' = z_o + D/2$, $z_o = 4.125D$. Black and pink markers, streamwise location of the turbine rows; blue dashed line, boundary of the COI.

2. *Coherence height*

In order to understand the vertical variation of the coherence of velocity fluctuations in the region in and around the rotors, we calculate $\rho_{\mathcal{W}_\psi[u'_i,u'_j]}(k_x, x, z, z')$ with varying z, z'. To assess a cumulative effect on the vertical correlation across the wind farm domain, we focus on the streamwise-averaged coherence defined as $\bar{\rho}_{\mathcal{W}_\psi[u'_i,u'_j]}(k_x, z, z') = \frac{1}{L_x}\int_{x_{\min}}^{x_{\max}} \rho_{\mathcal{W}_\psi[u'_i,u'_j]}(k_x, x, z, z')\mathrm{d}x$.

Since the coherence function $\rho_{\mathcal{W}_\psi[u'_i,u'_j]}$ is a nondimensional quantity, we are interested in associating a length scale similar in spirit with the integral length scale in the vertical direction within the certain span. This is further illustrated in the plots involving "coherence heights" (Fig. 12). We define this length scale, or the coherence height $H_{u'_i,u'_j}$, analogous to the definition noted in [60]:

$$\left[H_{u'_i,u'_j}(\lambda_x, x)\right]^2 = \int_{z_1}^{z_2}\int_{z_1}^{z_2} \rho_{\mathcal{W}_\psi[u'_i,u'_j]}(k_x, x, z, z')\mathrm{d}z\mathrm{d}z'. \tag{22}$$

The streamwise-averaged coherence height can be analogously defined as

$$\overline{H}_{u'_i,u'_j}(\lambda_x) = \frac{1}{L_x}\int_{x_{\min}}^{x_{\max}} H_{u'_i,u'_j}(\lambda_x, x)\mathrm{d}x. \tag{23}$$

Depending on the region of interest, the integration limits z_1, z_2 in Eq. (22) can be adjusted [60]. In the current paper, the coherence height in the turbine rotor region, $\overline{H}_{r,\,u'_i,u'_j}(z_1 = z_h - D/2, z_2 = z_h + D)$, is compared to the coherence height in the inner layer, $\overline{H}_{i,\,u'_i,u'_j}(z_1 = 0.1D, z_2 = 0.5D)$ (see Fig. 12). Note that $z_h - D/2 = 0.5D$, so the two regions of integration are adjacent.

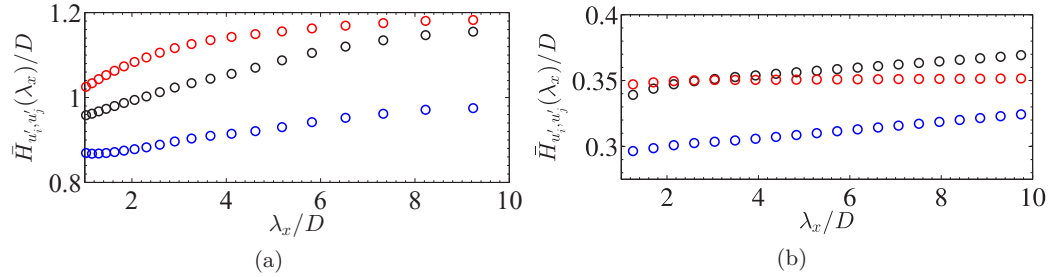

FIG. 12. Variation of the streamwise-averaged coherence height $\overline{H}_{u'_i,u'_j}(\lambda_x)$ with wavelengths. Black, $u'_i = u', u'_j = u'$; red, $u'_i = w', u'_j = w'$; blue, $u'_i = u', u'_j = w'$. (a) $\overline{H}_{r,\,u'_i,u'_j}(\lambda_x)$ in the rotor region (integration limits $z_1 = z_h - D/2, z_2 = z_h + D$). (b) $\overline{H}_{i,\,u'_i,u'_j}(\lambda_x)$ in the inner layer (integration limits $z_1 = 0.1D, z_2 = 0.5D$).

Figure 12 shows that, first, the coherence height in both regions is consistently lower than the integration span, confirming that the length scales are not truncated by the finiteness of the integration domain. The coherence height in the rotor region [Fig. 12(a)] varies between $0.8D$ and $1.2D$ and shows a strong correlation of structures all throughout the rotor width. Moreover, the plots show a steady growth in coherence height for u', w', and $u'w'$ correlations with the streamwise length scale, testifying to the strengthening of the large-scale motions on the order of the interturbine distance by wind turbines as noted above. The coherence height is the largest for the vertical velocity, followed by a streamwise velocity and by $u'w'$ correlation, showing the dominant role of the vertical motions in the energy transfer across the rotor region. On the other hand, a coherence height in the inner layer [Fig. 12(b)] (1) is on the order of $0.3D$–$0.35D$ (70% of the integration length, compared to the 85% of the integration length in the rotor region), (2) does not show a dominance of the correlated vertical motions (interestingly a lack of vertical mixing in the inner layer was also reported in the preliminary analysis of the recent field measurements in [61]), and (3) does not show a growth with λ_x for vertical correlations which are saturated at $0.35D$ at all length scales.

V. CONCLUDING REMARKS

The current paper focuses on investigation of spatial inhomogeneities in a spectral content of the energetic turbulent motions in a developing wind farm flow. For this purpose, a wavelet spectral analysis is performed on the spatially varying turbulent quantities, that allows us to decouple the spatial location and the spectral content of the inhomogeneous signals. We observe a significant growth of length scales for both streamwise and vertical velocity fluctuations after the first row of turbines, especially in the rotor region and in the outer layer of the atmospheric boundary layer. Wavelet intermittency function in a streamwise direction shows a significant amplification of energy in the length scales around $10D$ for both streamwise and vertical velocity fluctuations. The energy peaks at the length scales of $7D$ for streamwise velocity fluctuations, which coincide with the streamwise interturbine separation length, while a broader range of scales is seen to contribute to the energetic vertical motions. The vertical coherence plots signify that the motions of the order of $10D$ are also strongly correlated in the vertical direction, both for the streamwise and vertical fluctuations. It can also be observed that the u' fluctuation energy peaks at the narrow band of length scales slightly less than $10D$ between the second and third rows of turbines, while the energy in w' fluctuations, encompassing a broader region of scales of motion, peaks downstream of a wind farm.

The observed picture testifies to a formation of intermediately large-scale motions, on the order of $10D$, spurred by the presence of wind turbines in the atmospheric boundary layer. The evidence of the formation of the large-scale structures as early as past the first row of turbines is supported by the current data. One of the main conclusions of the current study is that not only streamwise but also vertical velocity correlations are enhanced in large scales after the first row of turbines. Enhancements of vertical velocity correlations is associated with the enhancement of the vertical momentum transfer between the outer layer and the wind turbine region, the so-called downdrafts of the mean kinetic energy [7,8]. This mechanism was previously observed in fully developed wind farms [7,8]. From a wind farm energetics perspective, it is associated with the energy extraction by wind turbines from the energetic motions in the outer layer that are brought down to the wind turbine level via the downdraft mechanisms. A significance of the current study is in demonstrating that this mechanism starts developing early in the wind farm and is likely associated with the (intermediately) large-scale motions created due to the interaction of wake turbulence with the boundary layer turbulence. While the energy associated with the downdrafts shows its peaks right downstream of the wind farm, the signature of strongly correlated motions in a streamwise and vertical direction persists far into the wake of wind farms, showing that the created large-scale motions are significantly robust and are not easily dissipated. This is in line with the previous studies that showed a persistence of the wind farm wakes for as long as $\sim$50 km downstream of a wind farm [62].

TABLE III. Summary of the geometry and computational grid parameters for the different cases simulated. Each case contains a 3×3 array of wind turbines. λ_R is the tip-speed ratio, and s_x is the streamwise distance between the turbine rows.

Case	Geometry	$N_x^e \times N_y^e \times N_z^e$	Grid points
$\lambda_R^3 s_{x,7D}$	$10\pi D \times 5\pi D \times 5D$	48×32×24	1.281×10^7
$\lambda_R^5 s_{x,7D}$ (baseline)	$10\pi D \times 5\pi D \times 5D$	48×32×24	1.281×10^7
$\lambda_R^8 s_{x,7D}$	$10\pi D \times 5\pi D \times 5D$	48×32×24	1.281×10^7
$\lambda_R^5 s_{x,3.5D}$	$10\pi D \times 5\pi D \times 5D$	51×32×24	1.361×10^7

While this work focuses on the analysis of the intermediately large scales of motion, between D and $10D$, future work could target an investigation of the interaction between the very-large-scale motions (VLSMs) with wind turbines, requiring significantly longer computational domains [3]. In addition to the long upstream domains to correctly capture the VLSM of an incoming ABL flow as in the work of [3], it would also be of interest to have a very long wind turbine domain and a downstream recovery region to capture the modulation of VLSMs by wind turbines and their subsequent reorganization.

ACKNOWLEDGMENTS

The authors T.C. and Y.T.P. would like to acknowledge the support of NSF-CBET Grants No. 1335868 and No. 1707075 and the computational time from XSEDE research allocations TG-ENG140005 and TG-ENG150019 for the work presented in the current paper. This work was done during T.C.'s association with Arizona State University as a graduate student.

APPENDIX A: COMPARISON OF STREAMWISE CORRELATION LENGTH SCALES FOR DIFFERENT TIP-SPEED RATIOS AND TURBINE LAYOUTS

In the current section, we document the comparison of length scales for different tip-speed ratios and turbine layouts in a 3×3 wind turbine array. Table III summarizes the geometry and grid sizes used for the simulated cases. The simulation cases are labeled as $\lambda_R^\chi s_{x,\eta D}$, where $\lambda_R = \omega R/U_h = \chi$ is the tip-speed ratio (TSR) and $s_x = \eta D$ is the streamwise distance between the turbine rows. The lateral distance between the turbines remains $s_y = 3D$ for all the cases. While this section documents the influence of the tip-speed ratio and the turbine layout on the correlation length scales, the rest of the paper presents the data from the baseline case, $\lambda_R^5 s_{x,7D}$.

We compute length scales based on two different measures: (i) correlation length scales, which estimate the coherence of turbulent motions within a specified interrogation window, and (ii) mixing length scales based on the resolved turbulent kinetic energy and the subgrid scale dissipation. The correlation length scales are calculated as the integral of the correlation function as documented in Eqs. (16) and (17) in Sec. IV A.

The mixing length scales are defined as

$$L_{k,\varepsilon}^{\text{span}} = \left.\frac{\sqrt{\frac{2}{3}}k^{1.5}}{\varepsilon}\right|_{Y^{\text{span}}}, \tag{A1}$$

$$L_{k,\varepsilon}^{\text{disk}} = \left.\frac{\sqrt{\frac{2}{3}}k^{1.5}}{\varepsilon}\right|_{Y^{\text{disc}}}, \tag{A2}$$

where $k = \frac{1}{2}(\widetilde{u}^2 + \widetilde{v}^2 + \widetilde{w}^2)$ is the resolved turbulent kinetic energy and $\varepsilon = -\tau^{SGS}\nabla^s\widetilde{\mathbf{u}}$ is the SGS dissipation [see Eq. (2) for the definition of τ^{SGS} and $\nabla^s\widetilde{\mathbf{u}}$]. The mixing length scale elucidates the

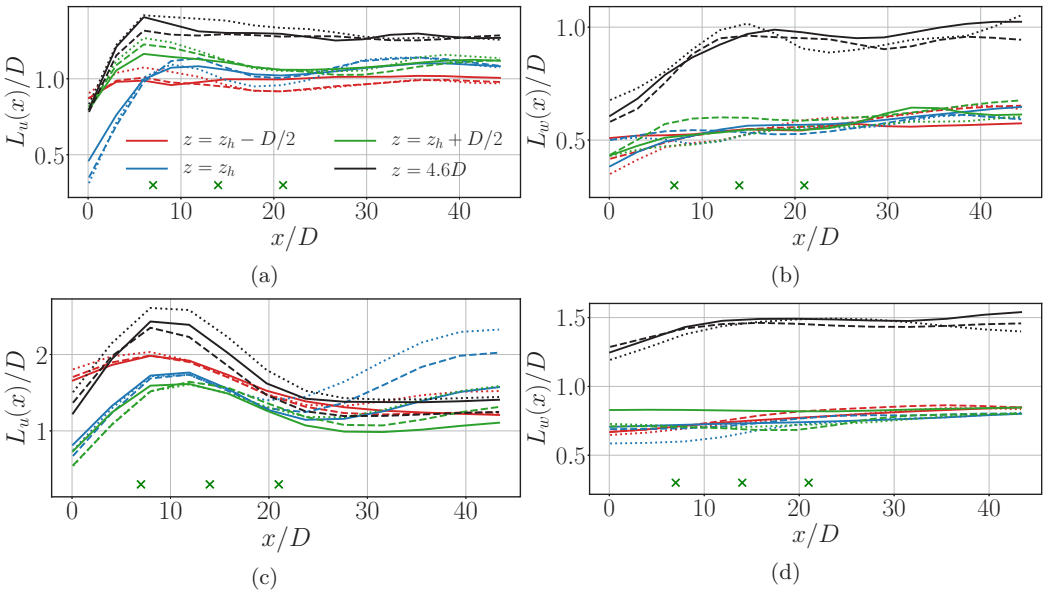

FIG. 13. Moving window correlation-based length scales [Eq. (17)] at different heights for the different cases simulated as in Table III. Solid lines, $\lambda_R^3 s_{x,7D}$; dashed lines, $\lambda_R^5 s_{x,7D}$; dotted lines, $\lambda_R^8 s_{x,7D}$. L_u and L_w, length scale based on streamwise and vertical velocity correlation. (a) L_u, window size $= 0.2L_x$, overlap $=$ 20%. (b) L_w, window size $= 0.2L_x$, overlap $= 20\%$. (c) L_u, window size $= 0.45L_x$, overlap $= 40\%$. (d) L_w, window size $= 0.45L_x$, overlap $= 40\%$. Green crosses denote the streamwise location of the turbine rows.

turbulent mixing of eddies that have a velocity scale $v_e \sim \sqrt{2/3\,k}$ and a turnover time scale $t_e \sim k/\varepsilon$. The superscripts *span* and *disk* in Eqs. (A1) and (A2) correspond to the averaging over a full span of wind farm, $Y^{\text{span}} = \{y : y_{\min} \leqslant y \leqslant y_{\max}\}$, and over the projection of the total area occupied by the turbine disks, $Y^{\text{disk}} = \cup_{i=1}^{3}\{y : y_{ci} - D/2 \leqslant y \leqslant y_{ci} + D/2\}$, where y_{ci} is the y coordinate of the center of wind turbines in the column $i = 1, 2, 3$, respectively.

Correlation length scales [Eqs. (16) and (17)] are documented in Figs. 13 and 14. From these figures, we observe that the correlation length scales depend both on the tip-speed ratio (Fig. 13) and the turbine layout (Fig. 14), with a general trend that higher tip-speed ratios and a tighter turbine layout (shorter interturbine distance) increase the correlation length scales.

In a calculation of the correlation length scales, we compare two different window sizes $0.2L_x$ and $0.45L_x$, with the overlap widths of 20% and 40%, respectively. A larger window size naturally captures larger length scales, but a precision of spatial localization of those scales is lower. From Figs. 13 and 14 it is observed that the streamwise growth of length scales upstream of a wind farm is consistently predicted by both windows in all the simulated cases, which testifies that this trend is significant in both u' and w' correlations and affects a variety of scales of motion. We hypothesize that the increase of length scales at the entrance and immediately upstream of the wind turbine array is associated with a blockage effect of the flow by wind turbines [63,64], which, in turn, results in a channeling and an acceleration of the local flow in between the turbines. It has been previously reported that flow acceleration causes an increase in turbulence length scales [65,66], which can be understood intuitively from considerations of vortex stretching. We observe that higher tip-speed ratios and a tighter layout intensify this phenomenon, at least in u' correlation scales, consistent with the notion that both higher tip-speed ratios and a tighter layout result in stronger turbine-flow interactions and stronger channeling effects.

The effect of the window size on the dip in u' correlation length scales past the first row of turbines, previously observed in the baseline case in Fig. 6, is pronounced. A smaller window of

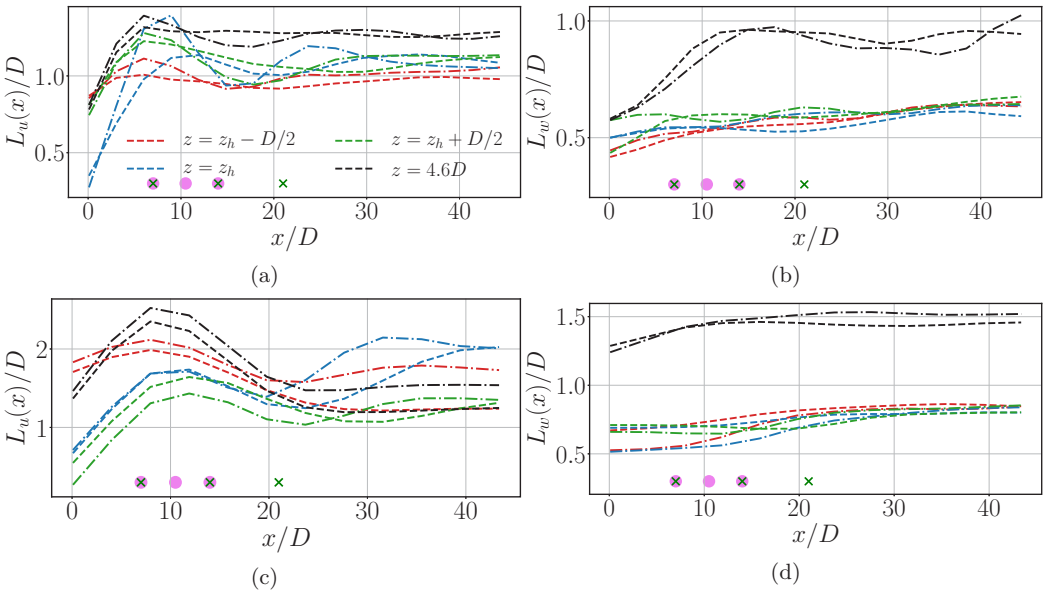

FIG. 14. Moving window correlation-based length scales [Eq. (17)] at different heights for the different cases simulated as in Table III. Dashed lines, $\lambda_R^5 s_{x,7D}$; dash-dotted lines, $\lambda_R^5 s_{x,3.5D}$. Variable specifications remain the same as in Fig. 13. Green crosses, wind turbine locations with $s_x = 7D$; pink circles, wind turbine locations with $s_x = 3.5D$.

$0.2L_x$ does not manifest this dip, which means that it is the larger scales of coherent motion that are being disrupted by the mixing processes and the interturbine interactions. The subsequent recovery of length scales at hub height downstream of a wind farm with the larger window size, previously observed in the baseline case, is even stronger for TSR = 8 and considerably weaker at TSR = 3, suggesting that these recovered length scales might be the signatures of the large-scale motions spurred by the turbine rotation. Expectedly, the length scale recovery with a shorter interturbine distance but the same TSR leads to an identical maximum of L_u/D values between $\lambda_R^5 s_{x,7D}$ and $\lambda_R^5 s_{x,3.5D}$ cases at the end of the domain, but recovery commences earlier in the $\lambda_R^5 s_{x,3.5D}$ case due to a shorter region occupied by wind turbines. Notably, a streamwise variation of length scales past the first row of turbines is captured in the $\lambda_R^5 s_{x,3.5D}$ case by both $0.2L_x$ and $0.45L_x$ windows, presumably because the shorter length scales are affected by this phenomenon due to a closer wind turbine spacing.

Compared to the length scales based on streamwise velocity fluctuations, those based on the vertical velocity fluctuations exhibit less dependence on the TSR and the turbine layout, a lack of length scale shortening past the first row of turbines, a fairly uniform streamwise distribution throughout the length of the wind farm and the wake, and a larger ratio of the length scale values in the outer layer to the values around the hub height, and top and bottom tips of the rotors. As discussed before, these increased correlations of the vertical velocity in the outer layer compared to the correlations in the rotor region likely represent the signatures of the large-scale downdraft motions, and are persistent across all simulated wind farm cases.

From the above discussion, it is seen that the windowed correlation length scales are subjective by definition, and a quantification of the variation of length scales depends on the window and overlap length. Consequently, we complement the analysis with another definition of length scales [Eqs. (A1) and (A2)], which relies on the local values of the turbulent kinetic energy and the SGS dissipation, thus avoiding the need for a windowed correlation.

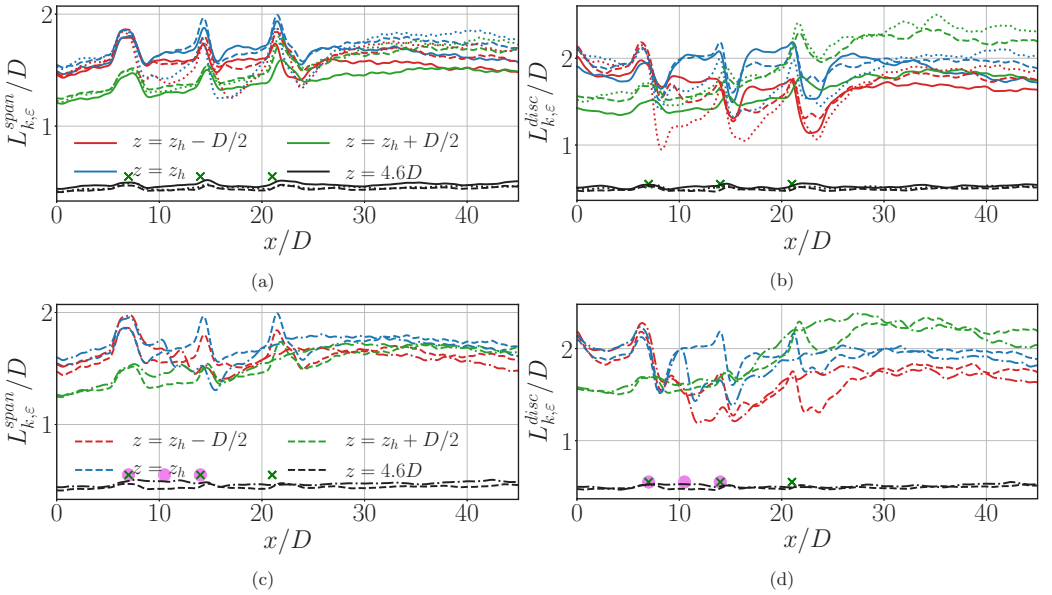

FIG. 15. Mixing length scales [Eqs. (A1) and (A2)] at different heights for the different cases simulated as in Table III. Solid lines, $\lambda_R^3 s_{x,7D}$; dashed lines, $\lambda_R^5 s_{x,7D}$; dotted lines, $\lambda_R^8 s_{x,7D}$; dash-dotted lines, $\lambda_R^5 s_{x,3.5D}$. Left: Spanwise-averaged correlation length scales. Right: Disk-averaged correlation length scales. Green crosses, wind turbine locations with $s_x = 7D$; pink circles, wind turbine locations with $s_x = 3.5D$.

It is interesting to note that the mixing length scales documented in Fig. 15 are of the same order of magnitude as the windowed correlation length scales. Unlike the windowed correlation length scales, however, the mixing length scales show much higher spatial variability, especially between the turbines, due to their local nature and a lack of dependence on the correlation window. Further, we note that when length scales are spanwise averaged, streamwise growth is observed in the upstream induction region, while for disk-averaged quantities, a slight dip is observed. This is in agreement with the fact that the channeling effect, occurring between wind turbine rows, is not captured by disk averaging, and, moreover, disk-averaging locations correspond to a region of a slightly decelerated flow, for which the turbulent length scales typically decrease [67]. This also explains a lack of well-defined peaks immediately upstream of wind turbines in disk-averaged quantities, while they persist in their spanwise-averaged counterparts. Furthermore, disk-averaged quantities capture stronger differences between the cases, since they sample exclusively in and around the wake regions, which are most significantly affected by the differences in a tip-speed ratio and a turbine layout. Both spanwise-averaged and disk-averaged mixing length scales consistently reveal stronger dips and a quicker recovery as the TSR is increased from 3 to 8 [Figs. 15(a) and 15(b)] and as the separation distance between the turbines is decreased from $7D$ to $3.5D$ [Figs. 15(c) and 15(d)], testifying to a stronger effect of mixing at higher tip-speed ratios and a tighter layout, as previously observed. Notably, mixing length scales assume very small values in the outer layer, as opposed to the correlation length scales, due to an evanescent role of mixing in the outer layer turbulence as exemplified by low levels of turbulent kinetic energy in these locations.

In summary, mixing length scales aim to represent the local state of turbulence and are able to capture sharp variations of scales of motion between the wind turbine rows. Correlation length scales, on the other hand, account for a spatial coherence between turbulent motions and aim to provide the information about larger, slowly varying eddies. Both length scales give a coherent picture that higher tip-speed ratios and a smaller interturbine distance intensify both the wake mixing

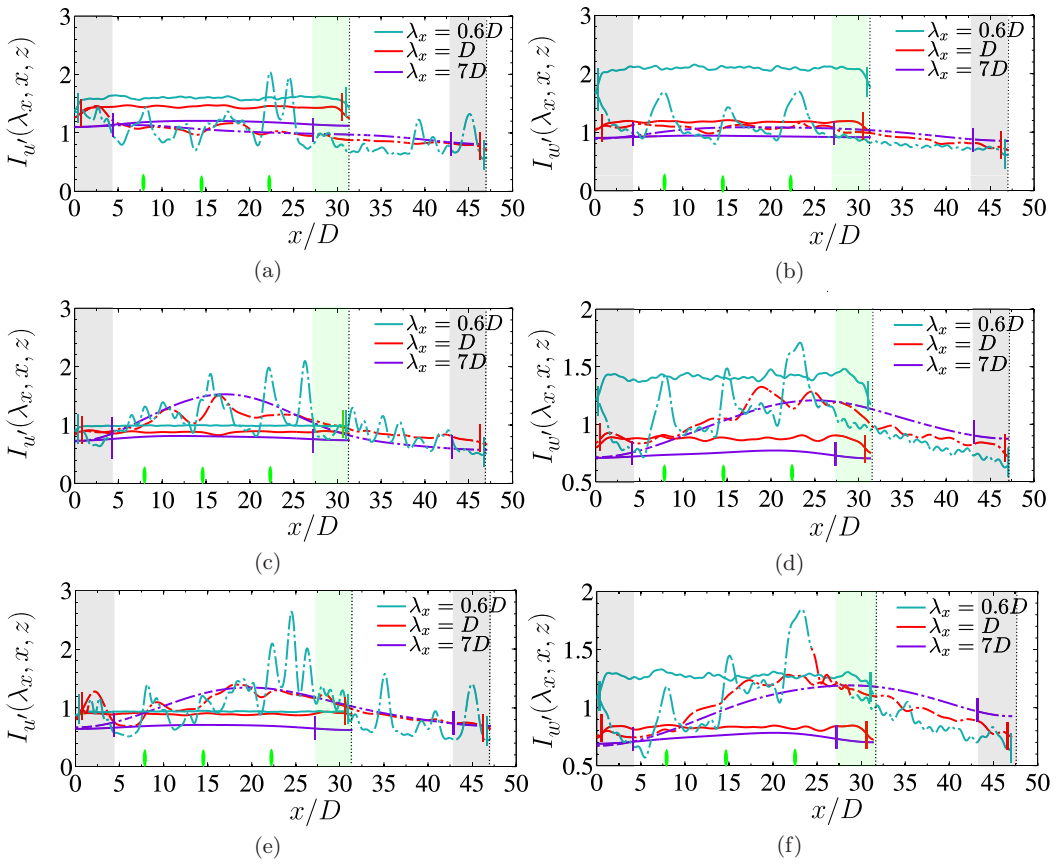

FIG. 16. Streamwise intermittency function of the WT array and the neutral ABL for (a), (c), (e) u velocity, $I_{u'}(\lambda_x, x, z)$, and (b), (d), (f) w velocity, $I_{w'}(\lambda_x, x, z)$. Both intermittency functions are normalized by the streamwise-averaged energy. (a), (b) $z = z_h - D/2$, bottom tip of the rotor; (c), (d) $z = z_h$, hub height of the rotor; (e), (f) $z = z_h + D/2$, top tip of the rotor. Solid lines, ABL domain; dash-dotted lines, WT domain. Color marks, boundaries of the COI for the WT and ABL domains. Gray or green patches, regions inside the COI of the wavelet with the maximum wavelength considered, $\lambda_x = 12D$ for the WT and ABL domains, respectively.

and the flow channeling effects, thus acting to increase the larger scales of motion outside the mixing region, and promote stronger variability in the near wake of wind turbines due to mixing effects.

APPENDIX B: COMPARISON OF WAVELET SPECTRA WITH NEUTRAL ABL

In Sec. IV B 1, we have considered an intermittency function of the wavelet u' and w' energy spectra in a wind turbine array, which is essentially a measure of a streamwise variation of the normalized wavelet spectra. To compare the wavelet energy spectra in the WT array to this in the neutral ABL flow, in this section we look at the relative wavelet spectra of the ABL flow normalized by the same value as the WT array wavelet spectra in Eq. (18); that is, we consider the following function:

$$I_\xi(\lambda_x, x, z)|_{ABL} = \frac{\widetilde{E}_\xi(\lambda_x, x, z)|_{ABL}}{\frac{1}{L_{xWT}} \int_{x\in\mathbb{R}} \widetilde{E}_\xi(\lambda_x, x, z)|_{WT}\, \mathrm{d}x}, \quad \xi = u', w'. \tag{B1}$$

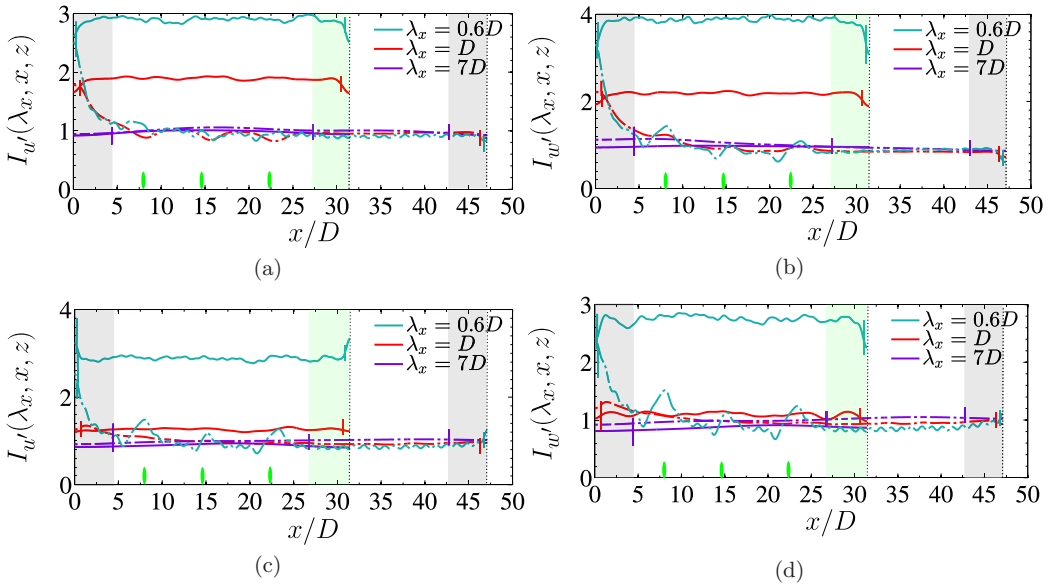

FIG. 17. Streamwise intermittency function of the WT array and the neutral ABL for (a), (c) u velocity, $I_{u'}(\lambda_x, x, z)$, and (b), (d) w velocity, $I_{w'}(\lambda_x, x, z)$. Both intermittency functions are normalized by the streamwise-averaged energy spectra of the WT array. (a), (b) $z = 0.125D$, inner layer; (c), (d) $z = 4.375D$, outer layer. Lines, color marks, and gray or green patches, same as in Fig. 16.

With a slight abuse of notation, we will call this function, defined by Eq. (B1), a neutral ABL "intermittency" function and plot it on the same plot with the WT array intermittency function in Figs. 16 and 17. We remark that this definition of the intermittency for the ABL domain does not yield an averaged value of one in a streamwise direction, but it serves judiciously as an indication of the relative strength between the wavelet spectral energy at the specified length scales between the neutral ABL and the WT cases.

The comparison of the intermittencies for the WT array and the neutral ABL cases is presented in Fig. 16 for the heights corresponding to the turbine rotor region in the WT array, and in Fig. 17 for the inner and outer layers. For clarity of the plots, only the scales $\lambda_x = 0.6D$, D, and $7D$ for both the neutral ABL and the wind farm cases are shown. It can be seen that the presence of wind turbines results in a significant reorganization of the boundary layer energetics compared to the neutral ABL case without wind turbines. The small-scale streamwise and vertical motions are significantly suppressed in the inner and outer layers. In the turbine rotor region, while the streamwise small-scale motions are essentially not effected, the vertical motions are still suppressed in the upstream portion of the wind farm. Past the first row of turbines, however, the energy in both the small and the large scales starts growing in the WT domain in the region of hub height through the top tip, ultimately reaching values higher than in the neutral ABL for the scales $\lambda_x \gtrsim D$. A suppression of the small scales in front of the wind farm can be related to the blockage and the channeling flow effects associated with the induction region of wind farms [63,64,66], and is consistent with our previous observation of a growth of length scales in the upstream portion of a wind farm discussed in Appendix A. The subsequent growth of energy in the small scales downstream of wind turbines is likely associated with the turbulent mixing in the turbine wakes, while the growth of large scales might be related to the development of global roll cell modes. We also remark that the neutral ABL spectra show significantly weaker variability in the streamwise direction at all length scales and at all heights as opposed to the WT spectra, as expected.

[1] J. N. Sórensen, R. F. Mikkelsen, D. S. Henningson, S. Ivanell, S. Sarmast, and S. J. Andersen, Simulation of wind turbine wakes using the actuator line technique, Philos. Trans. R. Soc. A **373**, 20140071 (2015).
[2] C. VerHulst and C. Meneveau, Large eddy simulation study of the kinetic energy entrainment by energetic turbulent flow structures in large wind farms, Phys. Fluids **26**, 025113 (2014).
[3] A. Önder and J. Meyers, On the interaction of very-large-scale motions in a neutral atmospheric boundary layer with a row of wind turbines, J. Fluid Mech. **841**, 1040 (2018).
[4] M. Zhang and R. J. A. M. Stevens, Characterizing the coherent structures within and above large wind farms, Boundary Layer Meteorol. **174**, 61 (2020).
[5] N. Hamilton, H. S. Kang, C. Meneveau, and R. B. Cal, Statistical analysis of kinetic energy entrainment in a model wind turbine array boundary layer, J. Renew. Sustain. Energy **4**, 063105 (2012).
[6] L. P. Chamorro, S. J. Lee, D. Olsen, C. Miliren, J. Marr, R. E. A. Arndt, and F. Sotiropoulos, Turbulence effects on a full-scale 2.5MW horizontal-axis wind turbine under neutrally stratified conditions, Wind Energy **18**, 339 (2015).
[7] T. Chatterjee and Y. T. Peet, Contribution of large scale coherence to wind turbine power: A large eddy simulation study in periodic wind farms, Phys. Rev. Fluids **3**, 034601 (2018).
[8] M. Calaf, C. Meneveau, and J. Meyers, Large eddy simulation study of fully developed wind-turbine array boundary layers, Phys. Fluids **22**, 015110 (2010).
[9] Y.-T. Wu and F. Porté-Agel, Atmospheric turbulence effects on wind-turbine wakes: An LES study, Energies **5**, 5340 (2012).
[10] P. K. Jha, E. P. N. Duque, J. L. Bashioum, and S. Schmitz, Unraveling the mysteries of turbulence transport in a wind farm, Energies **8**, 6468 (2015).
[11] L. P. Chamorro and F. Porté-Agel, A wind-tunnel investigation of wind-turbine wakes: Boundary-layer turbulence effects, Boundary Layer Meteorol. **132**, 129 (2009).
[12] T. Chatterjee and Y. T. Peet, Dynamics of large scale turbulence in finite-sized wind farm canopy using proper orthogonal decomposition and a novel Fourier-pod framework, Energies **13**, 1660 (2020).
[13] R. J. A. M. Stevens, D. F. Gayme, and C. Meneveau, Effects of turbine spacing on the power output of extended wind-farms, Wind Energy **19**, 359 (2016).
[14] G. Cortina, V. Sharma, and M. Calaf, Wind farm density and harvested power in very large wind farms: A low order model, Phys. Rev. Fluids **2**, 074601 (2017).
[15] I. Daubechies, *Ten Lectures on Wavelets* (Society for Industrial and Applied Mathematics, Philadelphia, 1992).
[16] Y. Meyer, *Wavelets and Operators* (Cambridge University Press, Cambridge, UK, 1993).
[17] F. Argoul, A. Arneodo, G. Grasseau, Y. Gagne, E. J. Hopfinger, and U. Frisch, Wavelet analysis of turbulence reveals the multifractal nature of the Richardson cascade, Nature (London) **338**, 51 (1989).
[18] J. Rupert-Felsot, M. Farge, and P. Petitjeans, Wavelet tools to study intermittency: Application to vortex bursting, J. Fluid Mech. **636**, 427 (2009).
[19] J. Kim, M. Bassenne, C. A. Z. Towery, P. E. Hamlington, A. Y. Poludnenko, and J. Urzay, Spatially localized multi-scale energy transfer in turbulent premixed combustion, J. Fluid Mech. **848**, 78 (2018).
[20] L. P. Chamorro and F. Porté-Agel, Turbulent flow inside and above a wind farm: A wind-tunnel study, Energies **4**, 1916 (2011).
[21] K. Dykes and R. Meadows, Applications of systems engineering to the research, design, and development of wind energy systems, NREL Technical Report No. NREL/TP-5000-52616 (2011).
[22] E. F. Baerwald, G. H. D'Amours, B. J. Klug, and R. M. R. Barclay, Barotrauma is a significant cause of bat fatalities at wind turbines, Curr. Biol. **18**, R695 (2008).
[23] A. Orell, D. Preziuso, N. Foster, S. Morris, and J. Homer, 2018 distributed wind market report, Pacific Northwest National Laboratory, U.S. Department of Energy, Office of Energy Efficiency and Renewable Energy (2018), https://www.energy.gov/sites/prod/files/2019/08/f65/2018%20Distributed%20Wind%20Market%20Report.pdf.
[24] T. Chatterjee and Y. Peet, Large eddy simulation of a 3×3 wind turbine array using actuator line model with spectral elements, AIAA Paper No. 2016-1988 (2016).

[25] Y. T. Peet and T. Chatterjee, The contribution of large scale structures in the power generation of finite scale wind farms using large eddy simulation, in *Proceedings of the 10th International Symposium on Turbulence and Shear Flow Phenomena (TSFP10)*, Chicago, USA, July 2017.
[26] P. Fischer, J. Lottes, D. Pointer, and A. Siegel, Petascale algorithms for reactor hydrodynamics, J. Phys.: Conf. Ser. **125**, 012076 (2008).
[27] M. O. Deville, P. F. Fischer, and E. H. Mund, *High-Order Methods for Incompressible Fluid Flow* (Cambridge University Press, Cambridge, UK, 2002).
[28] T. Chatterjee and Y. T. Peet, Effect of artificial length scales in large eddy simulation of a neutral atmospheric boundary layer flow: A simple solution to log-layer mismatch, Phys. Fluids **29**, 075105 (2017).
[29] S. B. Pope, *Turbulent Flows* (Cambridge University Press, Cambridge, UK, 2000).
[30] P. J. Mason and D. J. Thompson, Stochastic backscatter in large-eddy simulations of boundary layers, J. Fluid Mech. **242**, 51 (1992).
[31] J. W. Deardorff, A numerical study of three-dimensional turbulent channel flow at large Reynolds number, J. Fluid Mech. **41**, 453 (1970).
[32] U. Schumann, Subgrid scale model for finite difference simulations of turbulent flows in plane channels and annuli, J. Comput. Phys. **18**, 376 (1975).
[33] A. S. Monin and A. M. Obukhov, Basic laws of turbulent mixing in the ground layer of the atmosphere, Trans. Geophys. Inst. Akad. Nauk. USSR **151**, 163 (1954).
[34] T. Chatterjee and Y. Peet, Actuator line wind turbine simulations in atmospheric turbulent flows using spectral element method, AIAA Paper No. 2015-0727 (2015).
[35] N. Troldborg, Actuator line modeling of wind turbine wakes, Ph.D. thesis, Technical University of Denmark (2008).
[36] M. J. Churchfield, S. Lee, P. J. Moriarty, L. A. Martinez, S. Leonardi, G. Vijayakumar, and J. G. Brasseur, A large-eddy simulation of wind-plant aerodynamics, AIAA Paper No. 2012-0537 (2012).
[37] B. E. Merrill, Y. T. Peet, P. F. Fischer, and J. W. Lottes, A spectrally accurate method for overlapping grid solution of incompressible Navier Stokes equations, J. Comput. Phys. **307**, 60 (2016).
[38] T. Chatterjee, N. W. Cherukuru, Y. Peet, and R. J. Calhoun, Large eddy simulation with realistic geophysical inflow of Alpha Ventus wind farm: A comparison with LIDAR field experiments, J. Phys.: Conf. Ser. **1037**, 072056 (2018).
[39] R. J. Adrian, Structure of turbulent boundary layers, in *Coherent Flow Structures at Earth's Surface*, edited by J. G. Venditti, J. L. Best, M. Church, and R. J. Hardy (John Wiley & Sons, Chichester, UK, 2013), pp. 17–24.
[40] G. Pathikonda and K. T. Christensen, Inner-outer interactions in a turbulent boundary layer overlying complex roughness, Phys. Rev. Fluids **2**, 044603 (2017).
[41] R. B. Cal, J. Lebrón, L. Castillo, H. S. Kang, and C. Meneaveau, Experimental study of the horizontally averaged flow structure in a model wind-turbine array boundary layer. J. Renew. Sustain. Energy **2**, 013106 (2010).
[42] S. Dong, G. E. Karniadakis, and C. Chryssostomidis, A robust and accurate outflow boundary condition for incompressible flow simulations on severely-truncated unbounded domains, J. Comput. Phys. **261**, 83 (2014).
[43] T. Chatterjee and Y. T. Peet, Exploring the benefits of vertically staggered wind farms: Understanding the power generation mechanisms of turbines operating at different scales, Wind Energy **22**, 283 (2019).
[44] M. Farge, Wavelet transforms and their applications to turbulence, Annu. Rev. Fluid Mech. **24**, 395 (1992).
[45] J. Liandrat and F. Moret-Bailey, The wavelet transform: Some applications to fluid dynamics and turbulence, Eur. J. Mech. B: Fluids **9**, 1 (1990).
[46] R. M. Rao and A. S. Bopardikar, *Wavelet Transforms: Introduction to Theory & Applications* (Longman, 1998).
[47] L. Debnath, *Wavelet Transforms and Their Application* (Birkhäuser, Boston, 2002).
[48] P. Goupillaud, A. Grossmann, and J. Morlet, Cycle-octave and related transforms in seismic signal analysis, Geoexploration **23**, 85 (1984).

[49] C. Torrence and G. P. Compo, A practical guide to wavelet analysis, Bull. Am. Meteorol. Soc. **79**, 61 (1998).
[50] J. M. Lilly and S. C. Olhede, Higher-order properties of analytic wavelets, IEEE Trans. Signal Process. **57**, 146 (2008).
[51] B. J. Balakumar and R. J. Adrian, Large and very-large-scale motions in channel and boundary-layer flows, Philos. Trans. R. Soc. **365**, 665 (2007).
[52] N. Hutchins and I. Marusic, Evidence of very long meandering features in the logarithmic region of turbulent boundary layers, J. Fluid Mech. **579**, 1 (2007).
[53] J. M. Lilly, Element analysis: A wavelet based method for analysing time-localized events in noisy time series, Proc. R. Soc. London Ser. A **473**, 20160776 (2017).
[54] L. J. Lukassen, R. J. A. M. Stevens, C. Meneveau, and M. Wilczek, Modeling space-time correlations of velocity fluctuations in wind farms, Wind Energy **21**, 474 (2018).
[55] M. Farge, Y. Guezennec, C. M. Ho, and C. Meneveau, Continuous wavelet analysis of coherent structures, in *Studying Turbulence Using Numerical Simulation Databases. 3: Proceedings of the 1990 Summer Program*, Stanford University (1990), pp. 331–348.
[56] S. Xie and C. Archer, Self-similarity and turbulence characteristics of wind turbine wakes via large-eddy simulation, Wind Energy **18**, 1815 (2015).
[57] F. Porté-Agel, M. Bastankhah, and S. Shamsoddin, Wind-turbine and wind-farm flows: A review, Boundary Layer Meteorol. **174**, 1 (2020).
[58] A. J. Grinstead, C. Moore, and S. Jevrejeva, Application of the cross wavelet transform and wavelet coherence to geophysical time series, Nonlin. Process. Geophys. **11**, 561 (2004).
[59] D. Maraun, J. Kurths, and M. Holschneider, Nonstationary Gaussian processes in wavelet domain: Synthesis, estimation and significance testing, Phys. Rev. E **75**, 016707 (2007).
[60] J. Jiménez, J. Del Álamo, and O. Flores, The large-scale dynamics of near-wall turbulence, J. Fluid Mech. **505**, 179 (2004).
[61] C. L. Archer, S. Wu, A. Vasel-Be-Hagh, J. F. Brodie, R. Delgado, A. St. Pé, S. Oncley, and S. Semmer, The VERTEX field campaign: Observations of near-ground effects of wind turbine wakes, J. Turbul. **20**, 64 (2019).
[62] J. K. Lundquist, K. K. Duvivier, D. Kaffine, and J. M. Tomaszewki, Costs and consequences of wind turbine wake effects arising from uncoordinated wind energy development, Nat. Energy **4**, 26 (2019).
[63] K. L. Wu and F. Porte-Agel, Flow adjustment inside and around large finite-size wind farms, Energies **10**, 2164 (2017).
[64] J. Bleeg, M. Purcell, R. Ruisi, and E. Traiger, Wind farm blockage and the consequences of neglecting its impact on energy production, Energies **11**, 1609 (2018).
[65] M. Ichimiya, I. Nakamura, and S. Yamashita, Properties of a relaminarizing turbulent boundary layer under a favorable pressure gradient, Exp. Therm. Fluid Sci. **17**, 37 (1998).
[66] U. Piomelli and J. Yuan, Numerical simulations of spatially developing, accelerating boundary layers, Phys. Fluids **25**, 101304 (2013).
[67] Á. Tanarro, R. Vinuesa, and P. Schlatter, Effect of adverse pressure gradients on turbulent wing boundary layers, J. Fluid Mech. **883**, A8 (2020).